

Explaining Time Series Classifiers with PHAR: Rule Extraction and Fusion from Post-hoc Attributions

Maciej Mozolewski^{1,2*}, Szymon Bobek² and Grzegorz J. Nalepa²

¹Jagiellonian Human-Centered AI Lab, Mark Kac Center for Complex Systems Research, Jagiellonian University, Łojasiewicza 11, Krakow, 30-348, Poland .

²Department of Human-Centered Artificial Intelligence, Institute of Applied Computer Science, Jagiellonian University, Łojasiewicza 11, Krakow, 30-348, Poland.

*Corresponding author(s). E-mail(s): m.mozolewski@uj.edu.pl;
Contributing authors: szymon.bobek@uj.edu.pl;
grzegorz.j.nalepa@uj.edu.pl;

Abstract

Explaining machine learning (ML) models for time series (*TS*) classification remains challenging due to the difficulty of interpreting raw time series and the high dimensionality of the input space. We introduce *PHAR—Post-hoc Attribution Rules*—a unified framework that transforms numeric feature attributions from post-hoc, instance-wise explainers (e.g., *LIME*, *SHAP*) into structured, human-readable rules. These rules define human-readable intervals that indicate where and when decision-relevant segments occur and can enhance model transparency by localizing threshold-based conditions on the raw series. *PHAR* performs comparably to native rule-based methods, such as *Anchor*, while scaling more efficiently to long *TS* sequences and achieving broader instance coverage. A dedicated *rule fusion* step consolidates rule sets using strategies like *weighted selection* and *lasso-based refinement*, balancing key quality metrics: *coverage*, *confidence*, and *simplicity*. This fusion ensures each instance receives a concise and unambiguous rule, improving both explanation fidelity and consistency. We further introduce visualization techniques to illustrate specificity-generalization trade-offs in the derived rules. *PHAR* resolves conflicting and overlapping explanations—a common effect of the *Rashomon phenomenon*—into coherent, domain-adaptable insights. Comprehensive experiments on *UCR/UEA Time*

Series Classification Archive demonstrate that *PHAR* may improve interpretability, decision transparency, and practical applicability for *TS* classification tasks by providing concise, human-readable rules aligned with model predictions.

Keywords: Explainable AI (XAI), Time Series Classification, SHAP, LIME, Anchor, Rule-Based Explanations, Post-Hoc Explainability, Expert Knowledge Extraction, Feature Attribution, Rule Fusion, Human Interpretability, Deep Learning (DL)

1 Introduction

Explaining time series classifiers presents unique challenges compared to models for images or tabular data. Time series often lack obvious semantic features. Without domain expertise, even simple attribution outputs can be difficult to interpret, which complicates the use of standard *Explainable AI (XAI)* tools (Theissler et al. 2022). Temporal dependencies, phase shifts, and high dimensionality further worsens explanations. When non-specialized methods are applied, results can become unstable or overly generic (Gu et al. 2024). These issues reveal a key gap in current XAI research. Unlike non-temporal models built on intuitive, semantically rich features, time series classifiers demand explanations that both capture temporal dynamics and deliver meaningful, context-aware insights tailored to sequential data. Moreover, deep learning (*DL*) is widely used for time series (*TS*) classification, particularly in medicine and industry, because of its ability to model complex temporal patterns for tasks such as disease diagnosis and predictive maintenance. Despite strong predictive performance, these models remain hard to interpret in practice.

Aiming to address XAI challenges for state-of-the-art models such as *DL*, common approaches include numeric attribution methods like *Permutation Importance* (Altmann et al. 2010), *SHAP* (Lundberg and Lee 2017), and *LIME* (Ribeiro et al. 2016), as well as gradient-based techniques like *Saliency Maps* (Simonyan et al. 2013) and *Layer-wise Relevance Propagation (LRP)* (Bach et al. 2015), all of which quantify feature contributions and trace relevance through the model’s computations. These approaches facilitate feature ranking, sensitivity analysis, and model debugging by producing developer-oriented outputs like importance scores or heatmaps. However, studies show that such numeric explanations often highlight broad regions of the input without delivering clear, context-specific insights (Arsenault et al. 2024; Jin et al. 2021). In sequential data, this tendency gives rise to "*ambiguous rules*", where multiple time steps or variables appear equally influential and cannot be easily distinguished. Consequently, these explanations are difficult for non-experts to interpret (Jeyakumar et al. 2020; Rojat et al. 2021), and the challenge is amplified in *TS* classifiers, where temporal dependencies and the high dimensionality of multivariate sequences further obscure meaningful patterns (Schlegel et al. 2019; Theissler et al. 2022).

We preserve the strengths of numeric-based attribution methods: precise feature ranking, post-hoc interpretability, and local fidelity, while extending them to the time series classification domain. As a first step toward addressing these challenges, rule-based approaches provide a compact, human-readable alternative to

numeric attributions. We employ semi-factual reasoning to identify minimal temporal segments—interpretable intervals where perturbing feature values would not change the model’s prediction—thus generating concise, human-readable rules. Anchor rule-based explanations have demonstrated improved interpretability by extracting succinct *"IF-THEN"* conditions that align closely with model behavior (Ribeiro et al. 2018). However, such methods are seldom applied to *TS* data. Furthermore, rule-based methods become computationally prohibitive as sequence length increases (Arshad et al. 2024). Exhaustive search for stable *"IF-THEN"* conditions could be computationally infeasible, leading to a combinatorial explosion of candidate rules and temporal instability. Beyond computational infeasibility, Cognitive Load Theory, summarized by Skulmowski and Xu (2022), emphasizes reducing extraneous demands on human working memory. Analogously, simpler and unambiguous decision rules referencing a limited number of time steps minimize cognitive effort for experts, supporting interpretability and visualization by exposing time-localized, threshold-based conditions that can be inspected on the original signal.

Our motivation stems from the persistent difficulty of interpreting high-dimensional time series models with post-hoc methods, both attribution scores and rule-based. Moreover, existing work typically assesses single explainer separately, neglecting the advantages of fusing multiple sources and systematically evaluating their quality in terms of *coverage*, *confidence*, and *simplicity*. Finally, the opportunity to enhance transparency by overlaying explanations on time series plots has been largely overlooked. These gaps motivate our framework, which transforms *instance-level attributions* into concise, human-readable *rules*. Rather than relying on global XAI methods based on clustering or surrogate models (Mekonnen et al. 2024), our approach leverages numeric attributions such as *SHAP* (Lundberg and Lee 2017) and *LIME* (Ribeiro et al. 2016). We adopt *Anchor* (Ribeiro et al. 2018) as our baseline for comparison. Our framework unifies insights from diverse explainers, measures rule quality, and visualizes explanations directly on time series to facilitate transparent decision-making. Our framework primarily targets *TS* but can extend to structured data like tabular datasets.

PHAR aims to improve trust and transparency in *TS* classification with deep learning (DL) through three key contributions: (1) a pipeline that converts numeric post-hoc attributions into expert-level rule representations for *TS*; (2) a *fusion mechanism* that unifies rules from different explainers for better coherence and quality; (3) visualization of rules, as outlined in Figure 1. Each input time series is represented as a $T \times C$ matrix— T time steps t_1, \dots, t_T by C channels c_1, \dots, c_C —and is processed by a *deep learning classifier*. Post-hoc explainers such as *SHAP* and *LIME* compute numerical attributions. In the first stage, these outputs are converted into interval rules for each instance. Rule-based explanations such as *Anchor* can be used directly. In the second stage, rule sets derived from different explainers are fused using methods such as *union*, *weighted selection*, and *lasso-based refinement* to yield a single, coherent rule per instance. Finally, each rule is visualized as vertical interval markers overlaid on the original time-series plot, enabling domain experts to inspect

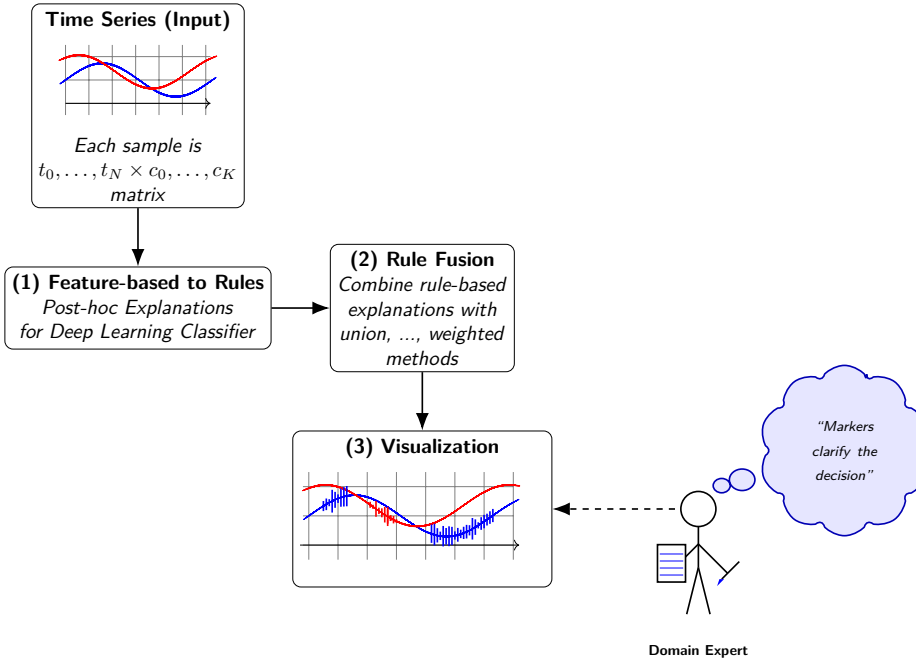


Fig. 1 Rules derived from post-hoc model explanations like SHAP.

and validate the model’s decision logic. Crucially, the visualization conveys information beyond the textual rule: it shows rule–signal alignment in time, overlap across channels and explainers, which supports faster error checking and expert validation.

The remainder of this paper is structured as follows: Section 2 reviews related work and explains our motivation. Section 3 details our framework, covering numeric-to-rule transformation (Section 3.3) and *fusion explainers* (Section 3.4). Section 4 evaluates coverage, confidence, and other metrics. Section 5 summarizes findings and future directions. The Appendix A provides supplementary tables, figures, and extended results, while "Supplementary Materials" (Section B) contains statical results for Critical Difference Diagrams.

2 Related work

In this section, we review the state of the art in time series explainability that informs our *PHAR* framework. TS explanation methods often use surrogate models like decision trees for rule-based intervals. *LIME* (Ribeiro et al. 2016), *SHAP* (Lundberg and Lee 2017), and *saliency maps* offer numerical insights but fail to capture temporal dependencies in TS. *DTW-based clustering* identifies prototypical patterns, providing structural insights. Studies explore *fuzzy rules*, *decision tree splits*, and *statistical impact rules*, emphasizing interpretability. Some methods balance rule complexity, local fidelity, and temporal coherence, while others focus on local or global views, leaving gaps in integrating both effectively. We first examine rule-based explanation

methods tailored to sequential data, and we then survey strategies for fusing multiple explainers.

Explaining TS classifiers is challenging, especially for complex models. [Mekonnen et al. \(2024\)](#) proposed a post-hoc method using *Parameterized Event Primitives* (PEPs) to explain TS models. Their approach detects key events (trends, extrema), clusters them, and derives rules via decision trees. These rules capture sequential patterns, supporting fidelity to model predictions and human interpretability, while acknowledging that such rules are proxies of model behavior rather than causal explanations. This method extracts meaningful patterns while maintaining temporal dependencies and lays the groundwork for hybrid explanations that address temporal dependencies.

[Spinnato et al. \(2023\)](#) propose a TS explanation framework combining saliency maps, instance-based examples, and rule-based methods. Saliency maps highlight key regions, instance-based methods provide prototypes and counterfactuals, and rule-based methods define logical conditions on subsequences. Integrating these methods bridges local and global explanations. This hybrid approach can improve interpretability and temporal coherence of the resulting explanations by constraining rules to compact time intervals and simple inequalities on the raw series.

Decision rules enhance interpretability in *TS* forecasting, especially in finance. [Arsenault et al. \(2024\)](#) review decision trees, fuzzy trees, and *Mamdani-type rules*. [Silva et al. \(2021\)](#) introduced *FDT-FTS*, combining fuzzy logic and decision trees for multivariate *TS* forecasting. *Mamdani-type rules* use fuzzy logic and linguistic variables for human-readable explanations. [Xie et al. \(2021\)](#) integrated them into the *Neural Fuzzy Hammerstein-Wiener network*. These methods balance predictive accuracy with human-readable simplicity of rules (few conditions, short intervals), supporting *TS* analysis. Next, we discuss decision rules for progressive decision-making.

The Belief–Rule–Based (BRB) framework ([Nimmy et al. 2023](#)) overcomes key weaknesses of post-hoc methods such as SHAP ([Lundberg and Lee 2017](#)), LIME ([Ribeiro et al. 2016](#)), and LINDA-BN ([Moreira et al. 2021](#)) by structuring explanations into human-readable rules. In the Knowledge Graph Module (KGM), expert input is formalized into a causal graph that captures both temporal order and inter-feature dependencies, addressing SHAP’s and LIME’s tendency to treat each timestep or feature independently and thus lose important sequence information. The Knowledge Propagation Module (KPM) then propagates belief distributions through this graph to extrapolate feature trajectories, inherently managing missing data and uncertainty without relying on expensive local sampling that can render SHAP and LIME at times unstable. Finally, the Feature Evaluation Module (FEM) synthesizes these propagated beliefs into concise *"IF–THEN"* rules that highlight the most influential intervals, removing the need to interpret raw attribution weights or fuzzy inference states as in LINDA-BN and enabling straightforward expert validation.

LIMREF ([Rajapaksha and Bergmeir 2022](#)) provides local, model-agnostic explanations for global *TS* forecasting models. It selects similar *TS* via DTW and generates synthetic instances via bootstrapping. Predictions guide impact rule derivation

using (Webb 2001). Rules fall into four types, including counterfactual and supportive, aiding forecast adjustments. By focusing on local TS neighborhoods, LIMREF ensures rules represent global model behavior. Its focus on local fidelity complements global and progressive methods.

Veerappa et al. (2021) apply interpretable association rule mining to TS classification in maritime settings. They evaluate surrogate models for rule-based explanations of a neural network classifier. Each method generates decision rules, balancing fidelity and complexity. They analyze how support thresholds and discretization bins affect explanation quality. The authors highlights trade-offs between rule complexity, accuracy, and interpretability, showing the role of hyperparameter tuning in domain-specific rule optimization.

Macha et al. (2022) introduced RuleXAI¹, an open-source rule-based explainability library for machine learning tasks. It supports classification, regression, and survival analysis by generating *elementary rule conditions* — simple threshold-based splits on individual features. RuleXAI provides both global and local explanations by directly learning interpretable models from data, without relying on black-box feature attribution methods. It transforms input data into binary feature conditions, reducing preprocessing complexity and ensuring high transparency. While not designed for time series data, RuleXAI’s symbolic rule extraction aligns with decision table logic and rule-based decision systems, facilitating straightforward human interpretability.

Hryniewska-Guzik et al. (2024) explore combining numeric feature-based XAI methods in an ensemble framework, though not for TS. They propose *NormEnsembleXAI*, which normalizes and aggregates explanations (e.g., feature-importance, local attributions) for consistent interpretability across models. Integrating LIME, SHAP, and Integrated Gradients, they show that uniform normalization reduces attribution variability and reveals coherent explanation patterns across models.

TSPProto by Bobek and Nalepa (2025) offers a complementary approach for explaining time series classifiers by converting feature attributions (e.g., SHAP or LIME) into high-level prototypes, which are then integrated into interpretable decision trees. However, it relies on a single XAI method to identify important regions and builds rules using a separate model based on SHAP-extracted features. As a result, it remains susceptible to the Rashomon effect, since in TSPProto SHAP only indicates potentially relevant regions, not how the model actually uses them in decision-making.

3 Method: Post-hoc Attribution Rules for time series

3.1 Overview of the *PHAR* Framework

The *PHAR* (*Post-hoc Attribution Rules for time series*) framework addresses the demand for semantically meaningful, stable, and cognitively efficient explanations in time series classification. In *PHAR*, we transform *post-hoc, instance-level numeric feature attributions* into concise, human-readable *rule-based explanations* and integrate outputs from multiple explainers enabling assessment of the quality of explanations

¹<https://github.com/adaa-polsl/RuleXAI>

and their visualization. First, *PHAR* selects the most salient temporal intervals—and, in multivariate settings, the most informative channels—so that rules focus on key patterns. Next, these intervals are translated into interpretable “*IF-THEN*” rules that preserve the model’s predicted class. An optional *fusion step* then merges rules from obtained from numeric attributions, Anchor explanations (Ribeiro et al. 2018), and potentially expert rules, optimizing for *coverage*, *confidence*, and *simplicity*. *Fusing* explanations via techniques such as *intersection*, *union*, and *weighted aggregation* ensures faithfulness to DL classifier predictions and usability for end-users. Finally, to reduce extraneous cognitive load, *PHAR* visualizes each rule with *semi-factual* plots that contrast actual and hypothetical behaviors, highlighting how small changes would affect the model’s decision. Our framework is structured around 4 Research Questions that guide the transformation, fusion, and visualization of rule-based explanations for time series classification.

RQ1: How can numeric attributions from *LIME* or *SHAP* be transformed into precise, interpretable *rule-based explanations* for *TS*?

RQ2: How can metrics like *coverage*, *confidence*, *feature count per rule*, and *explained instance percentage* help select a single, unambiguous rule representation and reveal explanation strengths and weaknesses?

RQ3: How can **fusion methods** combining rules from *LIME*, *SHAP*, and *Anchor* generate a single optimized rule per instance? Can this transformation also refine rules within a single explainer? Whether merging multiple perspectives into one rule per instance improves *coverage*, *confidence*, and *explanation ratio* without excessive complexity?

RQ4: How can visualizations support the interpretability of rule-based explanations in *TS* models? Rules may span multiple time steps and features (in *multivariate TS*). We explore whether overlaying rule-based explanations on *TS* plots helps illustrate their structure.

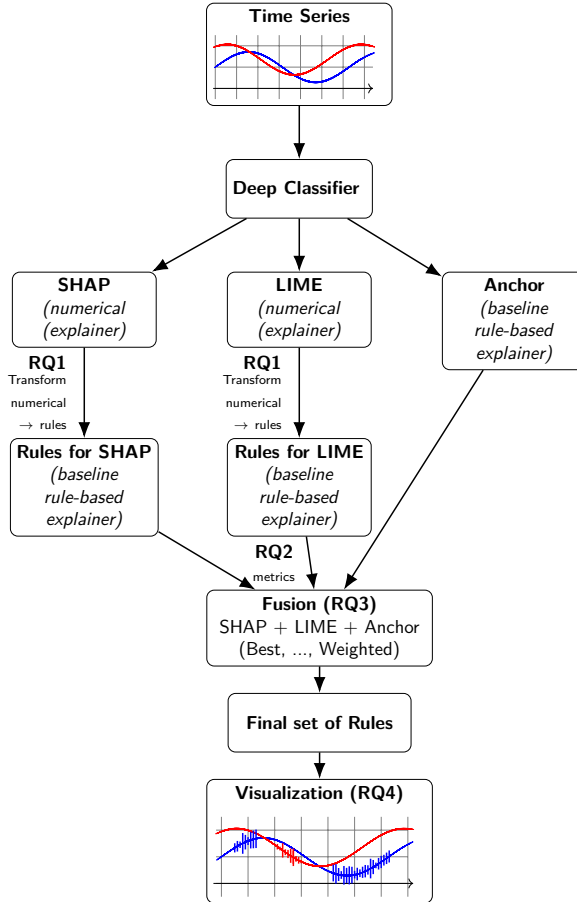


Fig. 2 Proposed framework with highlighted research questions RQ1...RQ4.

Figure 2 illustrates the *PHAR* framework with those Research Questions. A deep classifier first assigns each input series: univariate or multivariate, to a class. Post-hoc explainers *SHAP* and *LIME* yield numerical attributions that we convert into interval rules of the form $r : x_c^{(t)} \in (l_c^{(t)}, h_c^{(t)}] \Rightarrow \hat{y}, \text{conf}(r) = \gamma, \text{cov}(r) = \kappa$, where $x_c^{(t)}$ denotes "channel" c (in case of multivariate *TS*) at timestep t , $(l_c^{(t)}, h_c^{(t)}]$ is the selected interval, and γ, κ are the rule's confidence and coverage scores. This transformation addresses **RQ1** (Section 3.3). In parallel, *Anchor* generates rule-based explanations directly. We evaluate all candidate rules using metrics such as *coverage*, *confidence*, and *feature count* to address **RQ2** (Section 3.3.1). Then we apply multiple fusion strategies (*Intersection*, *Union*, *Weighted*, *Lasso*, *Lasso global*, and *Best*), controlled by these metrics, to select a single, optimized rule per instance (**RQ3**, Section 3.4). Finally, to support **RQ4**, we visualize each rule as vertical intervals overlaid on the original *TS*, highlighting feature–timestep relationships (Section 4.7 and Appendix A.4).

3.2 Rule-based explanations

In Davis et al. (1977), rules are expressed in the "IF-THEN" form augmented with a certainty factor. The premise is a conjunction of predicate evaluations $p_j(o_j, a_j) = v_j$ for $j = 1, \dots, n$, and the conclusion $q(o', a') = v'_{\text{out}}$ is drawn with a strength given by multiplying the aggregated premise confidence by CF_i :

$$R_i : \left(\bigwedge_{j=1}^n p_j(o_j, a_j) = v_j \right) \xrightarrow{\times \text{CF}_i} q(o', a') = v'_{\text{out}} \quad (1)$$

Here, p_j denotes a predicate function applied to object o_j and attribute a_j , v_j is its value, and the certainty factor CF_i quantifies the inference reliability. Building on this idea, we define our PHAR expert-system rule format as in (Ligeza 2006; Niederliński 2013), where each rule R_i comprises a set of logical conditions W_1, \dots, W_n , a conclusion W_{out} , and an inference semaphore S_i representing the combined confidence c_i obtained with the method described in Section 3.3.1:

$$R_i : \{W_1, W_2, \dots, W_n\} \xrightarrow{S_i} W_{\text{out}} \quad (2)$$

In this schema, each W_j is a logical condition derived from feature attributions, W_{out} is the predicted class or decision, and $S_i = c_i$ signals the rule's confidence.

Our approach follows established rule classifications in *knowledge-based systems* (Nalepa 2018). PHAR rules are best described as *derivation* and *classification rules*. *Derivation rules* define logical conditions under which a conclusion is inferred from given premises, in our case *TS* feature conditions leading to model predictions. *Classification rules* assign instances to classes based on these conditions. From the perspective of logical inference, our rules are *probabilistic deductive rules*. Deductive rules infer conclusions from premises. If premises hold, the conclusion follows deductively. Given a feature set and its constraints, our rules classify instances under a probabilistic confidence threshold rather than absolute certainty. Unlike classical deduction, our rules incorporate *confidence*, applying deterministically within probability constraints. Furthermore, our rules belong to *attributive rule languages* (Nalepa 2018). These languages encode *knowledge* via attributes and values, common in decision tables, rule-based systems, and databases. They enable intuitive representation and efficient manipulation. For example, the rule *if temperature($t = 10$) > 50 and pressure($t = 11$) < 10, then class = failure [$c = 0.85$]*, where $t = 11$ denotes the timestep index, provides a human-readable decision boundary that replaces raw numeric attribution scores.

Converting scores from explainers which produce raw *post-hoc numerical attributions*, such as SHAP and LIME, into a structured rule format makes it possible to compare and merge rules from different explainers, resolve conflicts when features are correlated, and engage *Domain Experts* in validating and refining the symbolic rules. Our approach employs *rule fusion* to aggregate rule sets produced by *post-hoc explainers* and additionally allows to incorporate *native rule-based explainers* like Anchor or even rules developed directly by *Domain Experts*. Inspired by ensemble methods (Dietterich 2000), we call this process **fusion** because it goes beyond classical bagging

or boosting. *Fusion* refines and unifies rules by weighting them according to *coverage*, *precision*, and *simplicity*, and by merging overlapping or redundant conditions. The resulting *fused rules* conform to the same *expert-system format*, allowing them to be easily evaluated, adjusted, visualized, and aligned with expert knowledge to support robust domain reasoning.

We illustrate a generic rule pattern for an arbitrary instance i as follows:

$$R_i : \begin{cases} t_{j_1} c_{j_1} \in (\ell_{j_1}, u_{j_1}] \\ t_{j_2} c_{j_2} \in (\ell_{j_2}, u_{j_2}] \\ \vdots \\ t_{j_k} c_{j_k} \in (\ell_{j_k}, u_{j_k}] \end{cases} \Rightarrow \begin{cases} \hat{y} = "A", \\ \text{CONF}(R_i) = \gamma, \gamma \in [0, 1], \\ \text{COV}(R_i) = \kappa, \kappa \in [0, 1]. \end{cases} \quad (3)$$

Here, each pair $t_{j_m} c_{j_m}$ denotes “channel” c_{j_m} (in multivariate series) at timestep t_{j_m} . The indices j_1, \dots, j_k are selected arbitrarily from the full set of T time steps and C “channels”, choosing the $k + 1$ pairs with the greatest impact on model predictions. Each interval $(\ell_{j_m}, u_{j_m}]$ has lower bound ℓ_{j_m} and upper bound u_{j_m} . $\text{CONF}(R_i)$ is the proportion of instances satisfying the rule that are correctly classified as class “A”, and $\text{COV}(R_i)$ is the fraction of all instances that satisfy the rule. The formal derivation of rules and their *CONF* and *COV* measures is presented in Sections 3.3 and 3.3.1, while Section 4.7 provides real-world examples of rules in this notation for selected dataset.

3.3 Conversion of numeric importance values to rules

We consider a TS dataset with N samples, univariate or multivariate, and a model generating multi-class predictions. In the univariate case, each feature f is indexed only by timestep, e.g. t_i , whereas in the multivariate case, features are indexed by both timestep and channel, e.g. $t_i c_v$. Let $\{X_n\}$ be instances with predicted classes y_n . Predicted classes serve as ground truth, as we focus on explanation consistency with DL model, not model accuracy itself. Feature-based explainers (e.g., *LIME*, *SHAP*) assign *numeric importance values* to each variable per timestep. Let $e_{n,f}$ denote importance values for instance n and feature f . To extract rules, we identify a threshold T (percentile-based) defining *important* features. Thresholds are computed per feature (*local*) or across all features (*global*).

We first compute absolute explanation values for all training instances and features. Let E be the multiset of absolute values: $E = \{|e_{n,f}| : n = 1, \dots, N, f = 1, \dots, F\}$, where $e_{n,f}$ is the explanation value for feature f (e.g., $t_i c_v$ for multivariate or t_i for univariate TS) at instance n . We then define a global threshold T_{global} by selecting a percentile p : $T_{global} = \text{Percentile}(E, p)$. If we apply thresholds per feature, we instead compute a separate threshold T_f for each feature f : $E_f = \{|e_{n,f}| : n = 1, \dots, N\}$, $T_f = \text{Percentile}(E_f, p)$. During inference on test instances, for each feature f , let $e_{n,f}$ be the explanation value for instance n :

$$\begin{aligned} & |e_{n,f}| \geq T_{global} \quad (\text{if using global thresholding; } \delta = \textit{True}), \\ \text{or } & |e_{n,f}| \geq T_f \quad (\text{if using per-feature thresholding; } \delta = \textit{False}). \end{aligned} \quad (4)$$

Features exceeding their threshold are *important*. For *important features*, we generate intervals preserving the model’s prediction. Stable intervals $(l_f, u_f]$ are derived via controlled perturbation of each *important feature* and sampling around $x_{n,f}$. Let F_* be *important features* for an instance, identified after thresholding. For each $f \in F_*$, we take the original value $x_{n,f}$ and generate perturbed samples: $x_{n,f}^{(m)} \sim \text{Uniform}(x_{n,f} - \Delta_f, x_{n,f} + \Delta_f)$, where Δ_f is a perturbation range based on training explanation statistics (std. deviation \times constant σ_p). Joint sampling over $f \in F_*$ captures nonlinear feature dependencies. For each perturbed sample $(x_{n,f}^{(m)})_{f \in F_*}$, we calculate the model’s prediction. Let $c_{ref}(n)$ be the original predicted class of instance n . If $c_{ref}(n) = y_n$, we determine $(l_f, u_f]$ per feature f preserving this class. Each $f \in F_*$ receives a stable interval: $f : x_f \in (l_f, u_f]$, defining a rule R_n for instance n :

$$R_n : \bigwedge_{f \in F_*} (x_f \in (l_f, u_f]). \quad (5)$$

This converts numeric importance into rule conditions with stable feature intervals.

3.3.1 Confidence and coverage of newly derived rules

After deriving the final rule R_n for instance n , we evaluate its explanatory quality on the test set. Consider the test dataset $\{X_{test,k}\}_{k=1}^{N_{test}}$, where N_{test} is the number of test instances. We identify the subset of test instances that satisfy the rule: $S(R_n) = \{X_{test,k} : X_{test,k} \text{ satisfies } R_n\}$. To measure coverage, we compute:

$$COV(R_n) = \frac{|S(R_n)|}{N_{test}}. \quad (6)$$

This ratio indicates how many test instances fall into the region defined by the rule’s intervals. A higher $COV(R_n)$ means the rule covers a larger portion of the test set.

To measure confidence, we focus on the consistency of predictions within $S(R_n)$. Let: $T(R_n) = \{X_{test,k} \in S(R_n) : y_{model}(X_{test,k}) = c_{ref}(n)\}$, i.e., the subset of covered test instances for which the model’s predicted class matches $c_{ref}(n)$. The confidence is then:

$$CONF(R_n) = \frac{|T(R_n)|}{|S(R_n)|}. \quad (7)$$

If no test instance satisfies the rule ($S(R_n) = \emptyset$), then $COV(R_n) = 0$ and $CONF(R_n)$ is undefined, meaning no explanatory power. However, at least instance n should satisfy the rule. If the rule covers test instances but does not match $c_{ref}(n)$, confidence decreases.

This procedure ensures *coverage* and *confidence* reflect how well derived intervals define a decision region on test data. High *coverage* means broad generalization; high *confidence* ensures alignment with model predictions.

3.3.2 Hyperparameter optimization in rule transformation step

To ensure that our rule-based explanations achieve a balance between fidelity and simplicity, we employ Optuna² (Akiba et al. 2019) to tune key hyperparameters of this step of our framework.

Optimized hyperparameters:

- p (*threshold percentile*): Percentile for feature importance thresholds. Higher values prioritize top-scoring features thus results in lower quantity of *important features*.
- δ (*global importance indicator*): Boolean for global or per-feature thresholding. If *True*, a single threshold T_{global} is applied; otherwise, thresholds T_f are computed per feature.
- σ_p (*perturbation scale*): Perturbation scale. Higher values widen the search for stable intervals.
- N_p (*perturbation samples count*): Number of perturbed samples for interval estimation. More samples improve precision but increase computational cost.

Optuna searches over the hyperparameters p , δ , σ_p and N_p to maximize objective on a held-out test set. During each trial, candidate configurations are evaluated by applying uniform sampling to estimate rule stability and decision region consistency, ensuring stable decision regions in the ML model’s input space. The best configuration is selected based on its performance on the test set, ensuring that the chosen thresholds generalize beyond the training data. Tuning these parameters balances feature selectivity, interval granularity, and computational cost. Table A1 (Appendix) summarizes hyperparameter ranges used in our study.

Specifically, we define an *objective function* maximizing *coverage* and *confidence* while penalizing empty or complex rules during *numeric explanations to rule transformation step* which is then feed to Optuna framework.

The objective function used in the optimization:

Each instance n starts with a complex rule from an explainer (e.g., *Anchor*, *LIME*, *SHAP*). Each rule defines intervals for features, e.g., timestep-channel $t_i c_v$ in multivariate TS or timestep t_i in univariate TS, denoted $F(R_n)$. Rules yield metrics: *coverage* $COV(R_n)$, *confidence* $CONF(R_n)$, and *count of features which rule specifies* $|F(R_n)|$. The initial *objective function* is:

$$M(n) = COV(n) \times CONF(n). \tag{8}$$

If rule for instance n is empty or absent, $M(n) = 0$. Otherwise, penalties are applied when certain thresholds are not met.

Then we introduce thresholds τ_{conf} , τ_{cov} , and τ_{feat} , which are chosen to balance rule quality and interpretability. τ_{conf} ensures a minimum confidence level for the rules, τ_{cov} prevents overly narrow rules by enforcing minimum coverage, and τ_{feat} limits the number of features in a rule to improve cognitive interpretability for end-users. We set $\tau_{conf} = 0.5$ because scikit-learn and many binary classifiers use 0.5

²Optuna: <https://optuna.org/>

as the default probability cutoff, aligning rule applicability with positive predictions above chance level and following standard model calibration practices. The coverage threshold $\tau_{cov} = 0.01$ (1% support) corresponds to the minimum support filter commonly adopted in association rule mining to remove infrequent patterns and ensure rule generality. We fix $\tau_{feat} = 10.0$ to limit the number of conjuncts per rule to at most ten, a choice motivated by default max-length settings in popular rule-mining libraries and grounded in human cognitive constraints defined by Miller’s Law (Miller 1956) of 7 ± 2 chunks for short-term memory.

$$M(n) := \begin{cases} M(n) \times \frac{CONF(n)}{\tau_{conf}}, & \text{if } 0 < CONF(n) < \tau_{conf}, \\ M(n) \times \frac{COV(n)}{\tau_{cov}}, & \text{if } 0 < COV(n) < \tau_{cov}, \\ M(n) \times \frac{\tau_{feat}}{Fcount(n)}, & \text{if } |F(R_n)| > \tau_{feat}. \end{cases} \quad (9)$$

These conditions are applied sequentially. The overall objective function is the average

over all N instances: $\bar{M} = \frac{1}{N} \sum_{n=1}^N M(n)$. Maximizing \bar{M} finds hyperparameters balancing $COV(n)$ (not too low) and $CONF(n)$ (not too low), avoiding empty solutions, and minimizing rule complexity.

3.3.3 Resolution of rules ambiguity

Several equally valid rules can be derived for a single instance and require subsequent resolution. When transforming numeric explanations into symbolic rules, different valid rules may arise depending on training data and hyperparameters. Consider three salient timestep–channel pairs $t_{j_1}c_{j_1}$, $t_{j_2}c_{j_2}$, and $t_{j_3}c_{j_3}$. The following interval rules for an arbitrary instance i might be derived:

$$R_{i,1} : \{t_{j_1}c_{j_1} \in (\ell_1, u_1]\} \Rightarrow \hat{y} = A, \text{ CONF}(R_{i,1}) = \gamma_1, \text{ COV}(R_{i,1}) = \kappa_1, \quad (10)$$

$$R_{i,2} : \{t_{j_2}c_{j_2} \in (\ell_2, u_2]\} \Rightarrow \hat{y} = A, \text{ CONF}(R_{i,2}) = \gamma_2, \text{ COV}(R_{i,2}) = \kappa_2, \quad (11)$$

$$R_{i,3} : \{t_{j_3}c_{j_3} \in (\ell_3, u_3]\} \Rightarrow \hat{y} = A, \text{ CONF}(R_{i,3}) = \gamma_3, \text{ COV}(R_{i,3}) = \kappa_3, \quad (12)$$

Here, each $t_{j_m}c_{j_m}$ denotes "channel" c_{j_m} (in multivariate series) at timestep t_{j_m} , each interval $(\ell_m, u_m]$ has lower bound ℓ_m and upper bound u_m , and $\gamma_m, \kappa_m \in [0, 1]$. Although $R_{i,1}$, $R_{i,2}$, and $R_{i,3}$ yield equivalent predictions due to temporal correlations in TS , rule ambiguity arises because explainers (e.g., *SHAP*, *LIME*) combined with hyperparameter-driven optimization select different variables. This optimization, which maximizes an objective defined in Section 3.3.2, resolves ambiguity within a single explainer by choosing, for example, $R_{i,shap}$ for *SHAP*-based attribution. However, the same procedure on *LIME* may produce $R_{i,lime}$. To handle these divergent explanations, in Section 3.4 we propose fusing the rule set $\mathcal{R}_i = \{R_{i,shap}, R_{i,lime}, R_{i,anchor}\}$ and selecting a single, optimized rule per instance.

3.4 Rule fusion across explainers

In rule-based systems theory (Ligęza 2006), combining rules is called *rule aggregation*. Our framework calls this *rule fusion*, as it *consolidates multiple rules into exactly one*

whenever possible. Unlike standard aggregation, our method also applies to a *single explainer*, assigning each instance a rule refined via metric optimization (e.g., **Lasso** method discussed later).

Let \mathcal{F} be the feature set and M are various explanations methods for *TS classification model* (e.g. rules obtained from *SHAP*). Features are indexed by f , each representing a timestep-channel pair (t, c) for multivariate TS, or timestep (t) for univariate TS. Explanations methods are indexed with m . Each method starts with multiple rules $R_i^{(m)}$ from different explainers m . Each rule contains feature conditions: $R_i^{(m)} = \{(f, (l_f^{(m)}, u_f^{(m)})) \mid f \in F_i^{(m)}\}$, where $(l_f^{(m)}, u_f^{(m)})$ is an interval for feature f . We propose the following *rule fusion* approaches:

Intersection: Only conditions present in *all* rules per instance are kept. For each feature f that appears in all $R_i^{(m)}$, we take the *narrowest* intersection of intervals:

$$R_i^\cap = \bigcap_m R_i^{(m)}. \quad (13)$$

In practice, if a feature f has intervals $(l_f^{(m)}, u_f^{(m)})$ in each rule, we take:

$$l_f^\cap = \max_m(l_f^{(m)}), \quad u_f^\cap = \min_m(u_f^{(m)}). \quad (14)$$

Union: All conditions appearing in any rule are included (instance wise). For features shared among multiple rules, we take the *broadest* union of intervals:

$$R_i^\cup = \bigcup_m R_i^{(m)}. \quad (15)$$

If a feature f has intervals from different rules, we set:

$$l_f^\cup = \min_m(l_f^{(m)}), \quad u_f^\cup = \max_m(u_f^{(m)}). \quad (16)$$

Weighted: We define a weight w_m for each method m , derived from a chosen metric (e.g., *confidence*). We compute a weighted presence of each feature and select only those exceeding a threshold τ :

$$\frac{\sum_m w_m \chi_f^{(m)}}{\sum_m w_m} > \tau \quad (17)$$

where $\chi_f^{(m)} = 1$ if feature f appears in $R_i^{(m)}$. For the selected features, intervals are combined by union.

Lasso and Lasso global: Each condition (feature-interval pair) is encoded as a binary $Z_{n,j}$, indicating if sample n meets condition j . We then solve:

$$\min_{\beta} \|y - Z\beta\|_2^2 + \lambda \|\beta\|_1. \quad (18)$$

Conditions with $\beta_j \approx 0$ are discarded, yielding sparser rules. **Lasso local**, **Lasso** for short, fits per instance; **Global lasso** finds conditions across all instances at once to find globally important conditions. Multiple conditions per feature are combined by union. If no rules exist for an observation in **Lasso global**, imputation is used. Rules are first collected per observation from different explainers (e.g., *SHAP*, *LIME*, *Anchor*). If no rule is assigned to an observation, the *most frequent rule in the predicted class* is used. If none exist, the *most frequent rule overall* is assigned as fallback. In **Lasso local** (later referred as **Lasso**) and other methods, observations without rules are excluded.

Best: We select the single rule that maximizes a chosen metric (e.g., confidence):

$$R_i^{\text{best}} = \arg \max_{R_i^{(m)}} (\text{metric}(R_i^{(m)})). \quad (19)$$

This approach avoids merging and simply picks the best-performing rule instance wise. **Finalization of resultant rules**: The *confidence* and *coverage* of newly derived rules are computed as described in Section 3.3.1 and added to each rule, quantifying how well the fused rule generalizes to the data.

4 Evaluation

4.1 Model architecture

All time series datasets were classified using a unified deep neural architecture based on stacked *ConvLSTM1D* layers. The input consisted of time series samples with shape (T, C) , where T denotes the number of time steps and C the number of "channels". For univariate datasets, $C = 1$. To capture both local and global temporal dependencies, each sequence was segmented into n_{steps} temporal blocks, where n_{steps} was chosen as the third smallest divisor of T , excluding 1 and 2. The segment length was computed as $n_{\text{length}} = T/n_{\text{steps}}$, resulting in an input shape of $(n_{\text{steps}}, n_{\text{length}}, C)$.

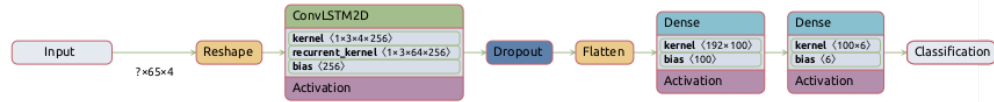


Fig. 3 Architectural overview of the ConvLSTM1D-based model used in the experiments.

The model architecture included two ConvLSTM1D layers with 64 and 32 filters, respectively, using a kernel size of 9 and ReLU activation. A dropout layer with a rate of 0.5 followed, then a flattening operation producing a fixed-length embedding. This was followed by two fully connected layers: a dense layer with 100 ReLU units and an output layer with softmax activation. Class imbalance was handled using computed class weights. The model was trained with the Adam optimizer, categorical cross-entropy loss, for 25 epochs with a batch size of 64. The same architecture was

used across all univariate and multivariate datasets without dataset-specific tuning. A random 75 : 25 train-test split was applied with stratification by class label.

A graphical summary of this architecture is shown in Figure 3, illustrating the flow from segmented TS input through ConvLSTM layers to the final classification output.

4.2 Computational complexity of PHAR

The computational cost of the proposed *PHAR* framework is primarily determined by two factors: the application of post-hoc explainers to time series data and the subsequent conversion of numeric attributions into symbolic rule representations and combining rules with fusion.

To provide a clear and structured analysis of computational complexity, we divide this discussion into three dedicated subsections, each corresponding to a major component of the *PHAR* pipeline. First, we evaluate the computational cost of the *base explainers*, such as *SHAP*, *LIME*, and *Anchor*, which generate the initial feature attributions or rule sets. Second, we analyze the cost of the *numeric-to-rule transformation*, which converts numeric explanations into human-readable symbolic rule intervals via perturbation-based sampling and interval search. Finally, we assess the complexity of the *rule fusion process*, which consolidates multiple rule sets into a single, optimized rule per instance.

4.2.1 Computational complexity of base explainers

SHAP explanations, based on kernel SHAP, have a computational complexity of $O(M^2)$, where M is the number of input features (Lundberg and Lee 2017). Exact SHAP computations are exponential ($O(2^M)$), but Kernel SHAP approximates Shapley values via weighted linear regression, which still scales quadratically with M ³.

LIME explanations involve sampling perturbed instances and fitting a local surrogate model (typically linear regression), resulting in complexity $O(S \cdot M)$, where S is the number of samples (Ribeiro et al. 2016). Further details are provided in the LIME documentation⁴.

Anchor explanations involve a beam search procedure over binary feature subsets, with complexity proportional to the size of the search space and sampling budget, typically $O(B \cdot S)$ where B is beam width and S sampling per candidate (Ribeiro et al. 2018), see appropriate github repository⁵.

4.2.2 Computational complexity of numeric-to-rule transformation

The *PHAR* pipeline performs two core steps: *thresholding* and *interval derivation*; and these are wrapped inside a *hyperparameter optimization* loop. PHAR repeatedly applies thresholding and interval generation to evaluate different parameter configurations, and once the best hyperparameters are selected, it executes those two steps one final time to produce the final rule set. In the following subsections, we first estimate

³<https://shap.readthedocs.io/en/latest/generated/shap.KernelExplainer.html>

⁴<https://github.com/marcotcr/lime>

⁵<https://github.com/marcotcr/anchor>

the computational cost of hyperparameter optimization (i.e., the number of repeated runs), and then analyze the individual complexities of the thresholding and interval derivation steps.

Hyperparameter optimization guides the selection of optimal threshold and perturbation settings. The search tunes four key parameters: the percentile threshold $p \in [50, 99]$, a binary flag $global \in \{\text{true}, \text{false}\}$, perturbation scale $\sigma \in [0.01, 1.0]$, and number of perturbation samples $S_p \in [1000, 10000]$ (see Table A1, Appendix). We use Optuna, a Bayesian optimization framework that adaptively explores this space and prunes unpromising trials early (Akiba et al. 2019). In the worst-case scenario: if no pruning occurs—the cost scales with the number of evaluated trials T , which can be as high as the total number of possible combinations in the Cartesian product of parameter ranges. However, due to pruning and adaptive sampling, the actual number of full evaluations is observed to be a small fraction of T . For practical use, PHAR allows bypassing this stage entirely by applying default settings, e.g., $p = 90$, $global = \text{true}$, making the optimization step optional.

Thresholding requires a linear pass over the explanation values with complexity $O(N \cdot F)$, where N is the number of instances and F the number of features.

Interval derivation constitutes the most computationally intensive step, with complexity scaling as $O(N \cdot F' \cdot S_p)$, where $F' \ll F$ denotes the average number of important features selected after thresholding, and S_p is the number of perturbation samples generated per instance. In practice, S_p is user-defined (typically ≤ 10000), and both the perturbation sampling and subsequent model evaluations are highly parallelizable. This keeps the overall runtime feasible for time series datasets of moderate size, such as those commonly found in the *UCR/UEA archives*, where N usually ranges from several hundred to a few thousand instances, and F corresponds to tens or low hundreds of input features Dau et al. (2019); Bagnall et al. (2018). This design ensures that PHAR remains computationally tractable on standard multi-core hardware.

4.2.3 Computational complexity of rule fusion

Rule fusion in PHAR uses lightweight aggregation strategies and adds negligible computational overhead compared to the previous steps.

Intersection, **Union**, and **Weighted** methods select the final rule for each instance by aggregating multiple candidate rules originating from different explainability sources. These methods rely on precomputed metrics embedded within the candidate rules (e.g., confidence, coverage) and do not require re-evaluation of the predictive model. Their computational cost scales linearly with the number of rule sources M and the number of explained instances N , resulting in an overall complexity of $O(N \cdot M)$. Since the number of candidate rule sources per instance is typically low (e.g., $M = 2$ or 3), this step introduces negligible overhead relative to earlier phases.

Lasso involves solving a sparse linear regression problem, scaling as $O(N \cdot F_r^2)$ for each instance or globally across the dataset. However, the rule matrix is highly sparse, allowing efficient optimization via coordinate descent (Tibshirani 1996). Overall, fusion contributes marginally to total computation time, with the primary bottleneck being the initial attribution computation.

4.3 Evaluation metrics and statistical testing

We compared the `baseline` explainers and fusions of two or three explainers. \bar{M} was applied as described in Section 3.3.2. The metric *ER* counts instances where the explainer generated rules in proportion to all cases. $\overline{\text{CONF}}$ and $\overline{\text{COV}}$, as in Section 3.3.2, were averaged over all instances. $\overline{F(n)}$ and $\text{Med}(F(n))$ represent the *mean* and *median* number of features in generated rules (for instances with rules). Furthermore, we defined composite metrics $\overline{\text{CONF}} \cdot \text{ER}$ and $\overline{\text{CONF}} \cdot \overline{\text{COV}} \cdot \text{ER}$, which combine *confidence*, *coverage*, and rule generation rates. To compare explainers and fusion methods statistical evaluation uses non-parametric *Friedman* test and post-hoc analysis with *Nemenyi* tests. Metrics are visualized for univariate and multivariate datasets to highlight key differences. Package *scikit-posthocs* (Terpilowski 2019) was used.

4.4 Setup: time series, explainers, and rule fusion

The datasets used in this study come from the *UCR/UEA Time Series Classification Archive*. Some multivariate datasets (e.g., *Libras*, *PenDigits*) originate from the *UCI* ML Repository but are used via their curated UCR/UEA⁶ versions (Dau et al. 2019; Bagnall et al. 2018). Our code is available at GitHub⁷ in the following notebooks: *UCR-explainers-lime-shap-anchor.ipynb*, *UCR-num2rules-optuna.ipynb*, *UCR-fusions-results.ipynb*.

We evaluated our methods on 43 datasets, including 81.4% univariate and 18.6% multivariate TS. These datasets cover diverse domains. For each dataset, a TensorFlow model classified TS samples, followed by explanations generated using Anchor, SHAP, and LIME at the variable (> 1 for multivariate) and time point levels. SHAP and LIME were converted into rule-based explanations using the process in 3.3.2. A separate test set, unseen during training, was used for evaluation. Table A2 summarizes datasets, including the number of features used in each dataset, explainers, fusion methods and resulting fused rule sets.

Anchor, LIME, and SHAP were primary baselines, forming the foundation for fused rule sets. Anchor was used in 58.1%, LIME in 65.1%, and SHAP in 62.8% of datasets. Fusion techniques (`Lasso`, `Weighted`) refined these explanations. `Lasso`, `Lasso global`, and `weighted` were applied to all 43 datasets (100.0%), while `Best`, `Intersection`, and `Union` were used in 62.8%. The latter methods were omitted when applied to a single baseline explainer since they would replicate its results. In contrast, `Lasso` and `Weighted` optimized rules even for individual explainers. As expected, the `Baseline` method appeared in all datasets (100.0%) as a reference. Fused rule sets combining two or three explainers were applied in 62.8% and 23.3% of datasets, respectively.

⁶UCR/UEA archive: https://www.cs.ucr.edu/~eamonn/time_series_data_2018/ and <https://www.timeseriesclassification.com/>. Selected datasets (e.g., *PenDigits*) originate from UCI: <https://archive.ics.uci.edu/>.

⁷<https://github.com/mozo64/papers/tree/main/phar/notebooks>

4.5 Evaluation of *fusion methods*

4.5.1 Pairwise and aggregated comparisons

Performance of baseline explainers: We evaluated *Anchor* and rules derived from *LIME* and *SHAP* under the **baseline** condition, representing their original, untransformed explanations. Unlike fusion methods that optimize rule structures, **baselines** reflect each explainer’s native performance. To compare them, we applied the *Wilcoxon signed-rank test* on matched datasets, ensuring robustness for non-normal data. Table A3 presents the statistical results, while Figure A1 visualizes the distribution of key metrics.

Comparison of fusions to *Anchor* baseline: We applied the *Wilcoxon signed-rank test* to compare fusion methods with individual explainers, considering two perspectives. Tables A4–A11 analyze fused rule sets, such as *Anchor+LIME* or *LIME+SHAP*, against the *Anchor baseline*. This evaluation determines whether combining multiple explainers improves key metrics.

Comparison of fusion methods to their respective baselines: Tables A12–A19 compare different fusion strategies, including **Lasso**, **Weighted**, and **Intersection**, to individual explainers like *Anchor*, *LIME*, and *SHAP*.

Visualization of comparisons: Figure A2 visualizes metric distributions, contrasting single explainers (orange) with fusion methods (blue) for \bar{M} , $\overline{\text{CONF}} \cdot ER$, $\overline{\text{COV}}$, and $F(n)$. Each boxplot includes mean, standard deviation, and median values. Additional plots detail results contrasting single explainers baseline with fusion explainers: Figure A3 (\bar{M}), Figure A4 ($\overline{\text{CONF}} \cdot ER$), Figure A5 ($\overline{\text{COV}}$), and Figure A6 ($F(n)$).

Median values of metrics: Table A20 reports the summary of median values, comparing rule sets derived from different explainers and their **fusions**, such as *Anchor* and *LIME+SHAP*, regardless of **fusion method**. Table A21 presents median values for different *fusion strategies* applied to explainers and their combinations, e.g. **Intersection**, **Weighted**,

4.5.2 Ranking-based and post-hoc analysis

Critical Difference Diagrams: CD diagrams rank methods across datasets based on their average performance. A lower rank generally indicates better results, as it corresponds to higher values of the evaluated metric, except for $F(n)$, where lower values are preferred, making higher ranks more desirable. Horizontal bars connect methods that do not differ significantly at $\alpha = 0.05$, while gaps denote statistically significant differences. Figure 4 presents CD diagrams for different fusion methods and baselines, ranking them according to their effectiveness across multiple metrics. Figure 5 extends the comparison to fused rule sets, showing how different explainers contribute to overall performance when used in combination. Additional figures in the appendix (Figures A7a–A7c) provide detailed comparisons for \bar{M} , ER , and $F(n)$, incorporating both explainer-level analysis (including individual explainers and their combinations) and specific fusion methods applied to these rule sets.

Detailed tables with Friedman and Nemenyi post-hoc comparisons are provided in "Supplementary Materials" (Section B) in Tables B22– B39.

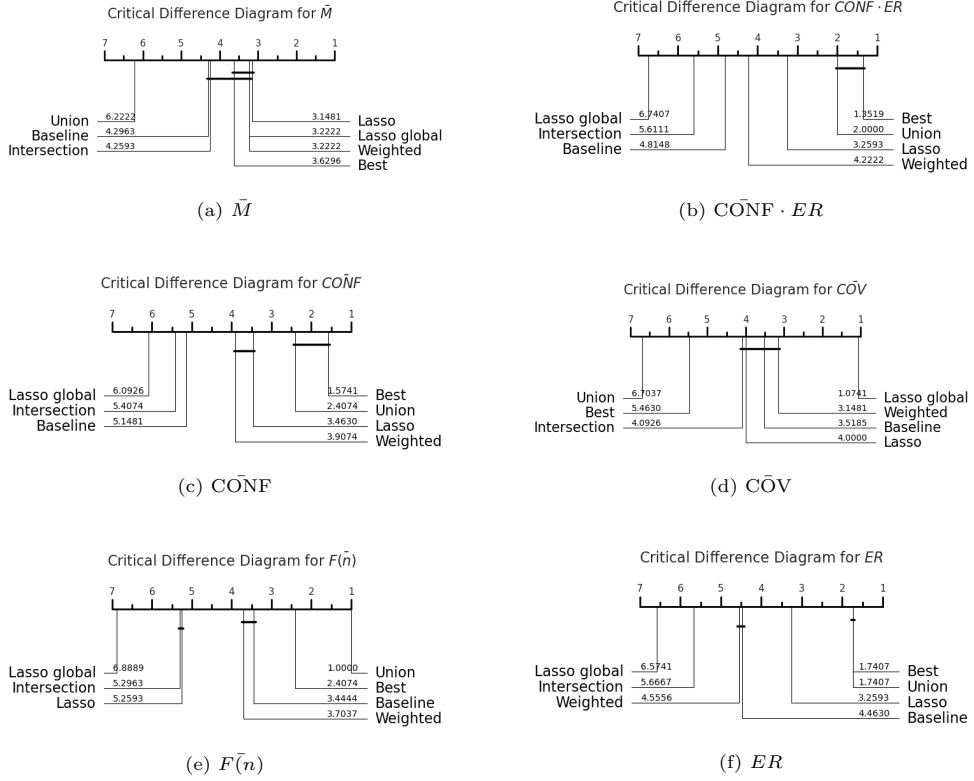


Fig. 4 Critical Difference Diagrams for selected metrics: (a) objective function \bar{M} , (b) $\overline{\text{CONF}} \times ER$, (c) $\overline{\text{CONF}}$, (d) $\overline{\text{COV}}$, (e) average feature count $F(\bar{n})$, (f) explained ratio ER . Methods joined by horizontal lines do not differ significantly at $\alpha = 0.05$.

4.5.3 Compound metrics \bar{M} , $\overline{\text{CONF}} \cdot ER$ and $\overline{\text{CONF}} \cdot \overline{\text{COV}} \cdot ER$

Using Wilcoxon signed-rank tests, we first evaluated the baseline performance of *Anchor*, *LIME*, and *SHAP*, confirming slight advantage of *Anchor*. Among *LIME* and *SHAP*, the latter performed better for $\overline{\text{CONF}} \cdot ER$. Next, we compared fusion methods to the *Anchor* baseline. For \bar{M} and $\overline{\text{CONF}} \cdot \overline{\text{COV}} \cdot ER$, fusions generally showed no significant gains, indicating that combining multiple explainers without considering the fusion method does not inherently improve results. However, when each fusion strategy was compared to its respective single-explainer baseline, we observed consistent improvements across all three compound metrics, with the best results from **Lasso**, **Weighted**, and **Best**. Other methods yielded comparable, worse, or statistically insignificant results. Friedman tests confirmed significant differences ($p < 0.05$) among both **fusion methods** and **explainer combinations**. Nemenyi post-hoc analysis further highlighted differences in performance, particularly for the best-performing methods. Critical Difference Diagrams (CDD) reinforced these findings, ranking **Lasso**, **Weighted**, and **Best** as the top fusion strategies. Among explainer combinations,

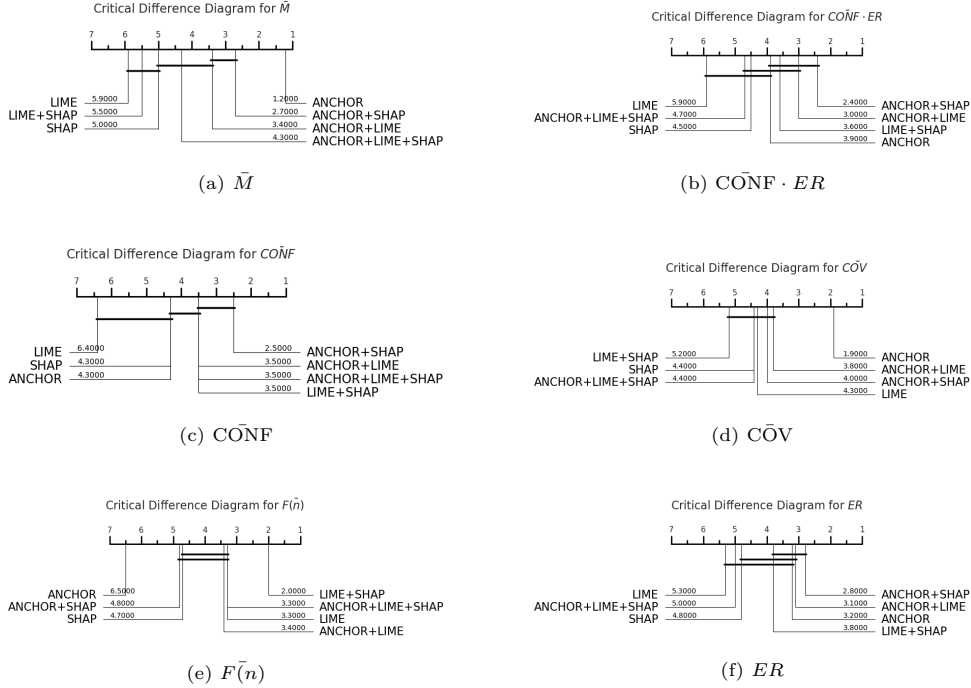


Fig. 5 Critical Difference Diagrams for selected metrics using fusion methods: (a) objective function \bar{M} , (b) $\overline{CONF} \times ER$, (c) \overline{CONF} , (d) \overline{COV} , (e) average feature count $\overline{F(n)}$, (f) explained ratio ER . Horizontal lines connect methods with no statistically significant differences ($\alpha = 0.05$).

Anchor and its fusions performed best, with *LIME+SHAP* achieving comparable results.

4.5.4 Confidence \overline{CONF} , Coverage \overline{COV} , and Explained Ratio ER

Wilcoxon signed-rank tests showed *SHAP* outperforming *LIME* in \overline{CONF} , while *Anchor+SHAP* exceeded *Anchor*. Most multi-explainer fusions improved \overline{COV} , but no significant differences were found for ER . Fusion methods **Best**, **Lasso**, **Union**, and **Weighted** consistently improved all three metrics over baselines. Friedman tests confirmed significant differences ($p < 0.05$), and Nemenyi post-hoc analysis validated the superior performance of these fusion methods. CDD illustrate these trends, ranking **Best**, **Lasso**, **Union**, and **Weighted** highest for \overline{CONF} , \overline{COV} , and ER . **Lasso global** excelled in \overline{COV} . Among explainer combinations, *Anchor*-based fusions ranked highest, with *LIME+SHAP* performing well for \overline{CONF} and ER .

4.5.5 Features Count $\overline{F(n)}$ and $\text{Med}(F(n))$

Wilcoxon signed-rank tests showed *Anchor* using the fewest features, with *LIME* generating fewer than *SHAP*. Against the *Anchor* baseline, all fused explainers had higher $\overline{F(n)}$ and $\text{Med}(F(n))$. Among fusion methods, **Intersection** and both **Lasso** variants minimized feature count, while **Union** (42.6 vs. 23.6) and **Best** (27.5 vs. 23.6) increased

it. Friedman and Nemenyi tests confirmed significant differences across methods and explainer combinations. CDD ranked **Lasso**, **Lasso global**, and **Intersection** as the most efficient in minimizing $\overline{F(n)}$, while *Anchor*, *SHAP*, and *Anchor+SHAP* ranked best in that regard among explainer combinations.

4.6 Summary of evaluation results

Anchor consistently performed best in \overline{M} and minimizing feature count, but was not dominant in $\overline{\text{CONF}}$, $\overline{\text{COV}}$, and *ER*. Among explainers, *SHAP* outperformed *LIME* in $\overline{\text{CONF}}$, and *Anchor+SHAP* surpassed *Anchor*. Most multi-explainer fusions improved $\overline{\text{COV}}$, while no significant differences were found for *ER*. Fusion methods had mixed effectiveness and choosing the right method is crucial. In compound metrics, **Lasso**, **Weighted**, and **Best** consistently improved performance. Some methods, such as **Union**, increased feature count significantly, while **Lasso** and **Intersection** minimized it. *CD Diagrams* confirmed that fusions often outperformed individual explainers. The best methods depended on the metric: **Lasso**, **Weighted**, and **Best** excelled in \overline{M} and compound metrics, while **Lasso global** was particularly effective in $\overline{\text{COV}}$. Among explainer combinations, *Anchor*-based fusions ranked highest, but *LIME+SHAP* also performed well in $\overline{\text{CONF}}$ and *ER*.

4.7 Qualitative evaluation

We illustrate PHAR on the *ECG200* dataset (two classes) using *observation 21*. Because the data are *univariate*, the channel index is omitted and rules refer directly to *time-step* indices. For LIME and SHAP we convert per-time-step attributions into contiguous interval constraints using the procedure in Sec. 3.3; *Anchor* provides a native rule set. We then form rule sets by three fusion operators (Sec. 3.4): *union* (all intervals from the inputs are pooled into one conjunctive rule), *lasso* (a sparse re-selection of intervals under an ℓ_1 penalty), and *best* (a single rule is chosen by a deterministic ranking: confidence has top priority; in a tie a fixed explainer order breaks ties).⁸ All values are standardised *z*-scores relative to the training set. Thus thresholds can be read as deviations from the mean, which makes the intervals actionable: one can see how much the signal would need to move to break or satisfy a condition. In practice, the interval conditions ($t_i \in [\ell, u]$) are contextualised as characteristic segments, such as an initial dip, a mid-sequence plateau or a terminal return to baseline—which makes the explanation more natural than a bare list of thresholds.

We recommend a two-step reading path. First, inspect the visualised intervals to understand *where* in the trace the decision is anchored. Second, examine the explicit rule statements to see the exact inequalities. We follow this order below.

Figure 6 shows the rule intervals for *observation 21*. The blue curve is the signal. Red dashed segments mark the time intervals required by each rule R_{21} . The numbers in each panel report confidence and coverage on the test set. Panels (a)–(c) present single-explainer benchmarks: *Anchor*, *LIME*, and *SHAP*. Panels (d) and (f) show *union* fusions: *Anchor+SHAP* and *LIME+SHAP*. Panels (e) and (h) show *lasso*

⁸Other tie-breakers, e.g. adding a sparsity term, are possible but not used here.

fusions: *LIME+SHAP* and *Anchor+LIME+SHAP*. Panel (g) reports the *best* selection over all explainers. We next discuss each panel in turn.

(a) *Anchor (benchmark)*. Two semi-infinite thresholds at t_{42} and t_{51} localise the decision in the mid/late part of the trace. The rule is extremely compact (high confidence, moderate coverage), but the one-sided nature of the thresholds provides little temporal extent, which limits shape specificity.

(b) *LIME (benchmark)*. Many short intervals concentrate in the mid section ($\approx t_{36}$ – t_{56}) and late flat portion, and LIME also flags the early inflection around t_{16} – t_{17} and another change near t_{22} . This pattern closely tracks local shape variations and attains full confidence at low coverage.

(c) *SHAP (benchmark)*. SHAP emphasises the initial drop (t_4 – t_6 , t_{10} – t_{11}) and the local peak/plateau around t_{22} – t_{30} . It therefore complements LIME by assigning more weight to the early and early-mid morphology.

(d) *Fusion (union): Anchor+SHAP*. The union operator pools all conditions from both inputs into a single conjunctive rule. In this instance the union has the same confidence and coverage as SHAP because every test case that satisfies SHAP’s intervals already satisfies Anchor’s mid/late thresholds, so the added Anchor conditions are redundant and the covered set is unchanged. Since adding conjunctive conditions cannot increase coverage and does not decrease it here, confidence also remains the same. The extra Anchor intervals mainly make the mid section explicit in the panel.

(e) *Fusion (lasso): LIME+SHAP*. Lasso reduces cognitive load by pruning overlapping or lower-priority intervals under the ℓ_1 selection criterion. The retained set remains balanced: it keeps informative early (from SHAP), mid (from both), and late segments (from LIME), yielding a concise yet representative rule.

(f) *Fusion (union): LIME+SHAP*. Pooling both explainers yields the most extensive set of intervals along the trace—dense mid/late coverage from LIME together with SHAP’s early emphasis. This gives a simple reading: early evidence is provided by SHAP and mid/late evidence by LIME, allowing a practitioner to probe “WHAT-IF” edits across substantial part of waveform. Adding intervals in a conjunctive rule can maintain or reduce coverage, but not inflate it.

(g) *Fusion (best): Anchor+LIME+SHAP*. For this observation, the *best* selector returns exactly the *LIME (benchmark)* rule. LIME achieves the highest confidence at the attained coverage. In this case SHAP attains the same metrics, but our deterministic tie-break (fixed explainer order) selects LIME, so SHAP is not chosen.

(h) *Fusion (lasso): Anchor+LIME+SHAP*. Lasso selects a sparse subset drawn from *all three* sources, without favouring a single explainer. The resulting rule captures dispersed early, mid and late segments while remaining sparse (compact).

To sum up, Anchor provides the shortest and most readable rule, but it is less useful in visual analysis: its one-sided, semi-infinite thresholds highlight isolated time indices rather than contiguous segments, so they convey little about waveform duration or shape. LIME and SHAP emphasise different phases (mid/late vs. early/early-mid). Union fusions offer the broadest spatial map of supporting intervals, whereas lasso fusions distil them to a compact subset. The *best* fusion method returns a single rule according to the stated priorities; in this case the selected rule is LIME, tied with SHAP on the metrics.

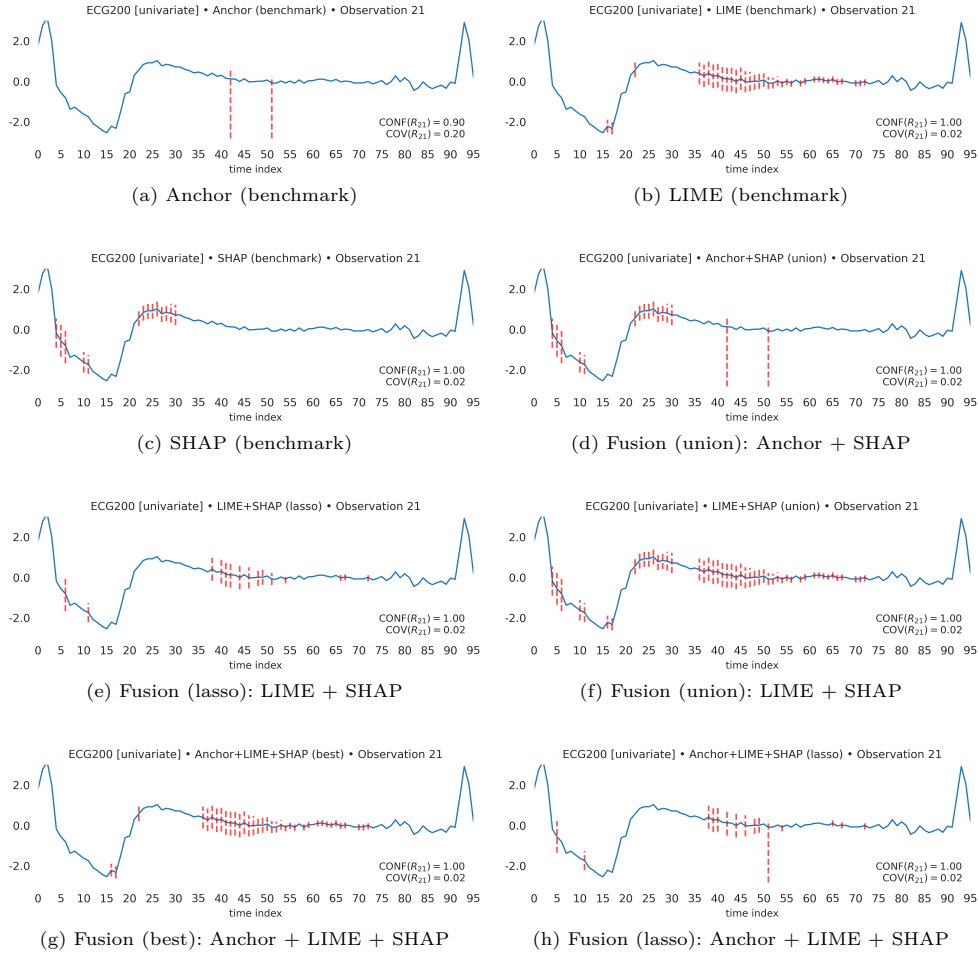


Fig. 6 Observation 21 from ECG200 dataset (univariate). Rule intervals produced by single explainers (Anchor, LIME, SHAP) and by various fusion strategies. The blue curve is the signal; red dashed bands mark the value intervals used by rule R_{21} for each method. Confidence and coverage are printed within each panel. Definitions of fusion methods are provided in Sec. 3.4.

4.7.1 Counterfactuals: testing rule boundaries

Counterfactuals help assess whether an instance-level rule genuinely separates classes in ways that are meaningful to practitioners. In our setting, a *counterfactual (CF)* is defined operationally: it is a *test* observation drawn from the *opposite* class and overlaid as a dotted trace. This construction is diagnostic rather than causal: it provides a direct visual contrast that lets experts see where and how the rule would be violated by an instance that should be rejected.

We use CFs to clarify what the rule demands and which time segments carry the decision. All series are shown in the same normalised scale. Red dashed segments indicate the admissible value ranges at specific, constrained time indices t ; these may

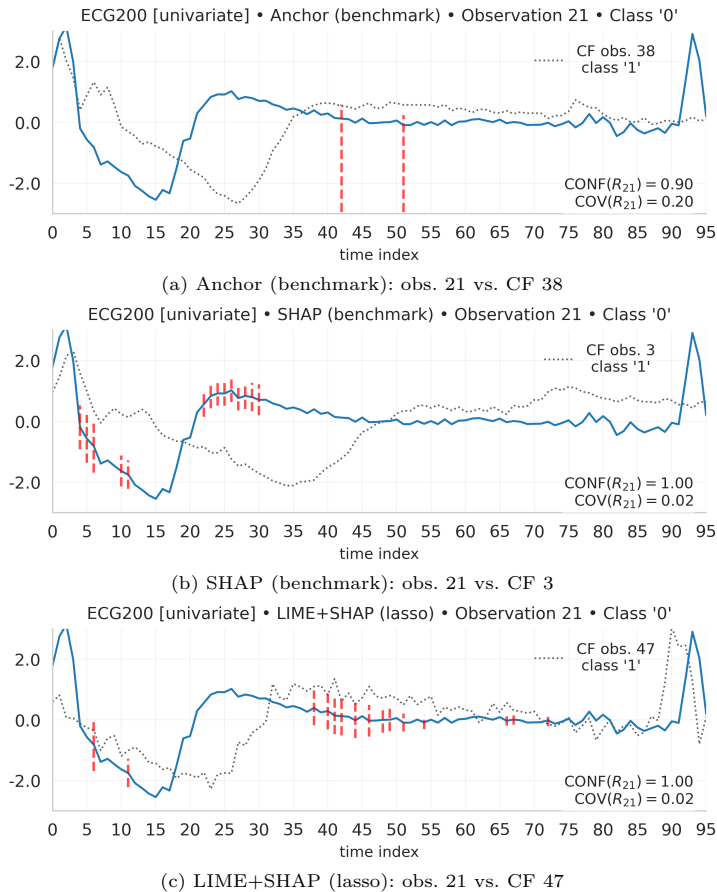


Fig. 7 Examples illustrate three Counterfactuals for instance 21: (a) Anchor (benchmark) with CF instance 38; (b) SHAP (benchmark) with CF instance 3; and (c) LIME+SHAP with lasso fusion with CF instance 47.

be two-sided intervals or one-sided thresholds. The blue curve (target observation) satisfies all marked ranges. The grey dotted CF does not: whenever the dotted trace exits a red segment at a constrained t , the rule is broken and the CF remains in the opposite class. A small box on each panel reports the rule's CONF and COV, which contextualise how reliable and how frequent the rule is across the test set. This combination—contrast against a CF, explicit intervals, and summary metrics—yields a compact, expert-friendly reading of the decision boundary.

The three panels tell a coherent story: CF leaves the admissible bands, which results in a class flip. In panel (a) *Anchor (benchmark)* imposes two mid-series intervals, around $t \approx 43$ and $t \approx 50$, with narrow bands slightly above zero; the target trace remains inside both, whereas the CF crosses them from above and thus violates the rule. In panel (b) *SHAP (benchmark)* concentrates on the early rebound after the initial dip ($t \approx 20$ – 27) and requires a short positive excursion; the target exhibits this burst, while the CF stays lower and repeatedly exits the band. In panel (c)

LIME+SHAP (lasso) selects a compact sequence of mid-section intervals ($t \approx 39$ – 60) centred near zero with a slight positive offset; the target stays within these tight corridors, whereas the CF drifts outside at several constrained times.

4.7.2 Rule listings for the panels

Guided by the rule intervals in Fig. 6 and Fig. 7, we now give the corresponding rule statements for panels (a)–(h). Each listing follows the same notation and uses standardised z -scores. Presenting visuals before equations aids time-series interpretation: the reader can first locate the relevant phases of the waveform and then verify the precise inequalities. Showing the inequalities after the visuals keeps the focus on *where* the decision is anchored and then makes it precise enough to audit or run simple "WHAT-IF" perturbations. This also facilitates counterfactual checks—one can perturb the signal within a highlighted window to test whether the rule would be violated. Panel labels are retained so the reader can cross-reference each rule with its subfigure.

a) *Anchor (benchmark)*

$$R_{21} : \begin{cases} t_{42} \leq 0.58 \\ t_{51} \leq 0.23 \end{cases}$$

$$\hat{y} = "0",$$

$$\Rightarrow \text{CONF}(R_{21}) = 0.90,$$

$$\text{COV}(R_{21}) = 0.20.$$

c) *SHAP (benchmark)*

$$R_{21} : \begin{cases} t_4 \in (> -0.92, \leq 0.52] \\ t_5 \in (> -1.36, \leq 0.21] \\ t_6 \in (> -1.69, \leq 0.04] \\ t_{10} \in (> -2.15, \leq -1.13] \\ t_{11} \in (> -2.22, \leq -1.28] \\ t_{22} \in (> 0.15, \leq 0.97] \\ t_{23} \in (> 0.43, \leq 1.23] \\ t_{24} \in (> 0.51, \leq 1.31] \\ t_{25} \in (> 0.51, \leq 1.31] \\ t_{26} \in (> 0.62, \leq 1.41] \\ t_{27} \in (> 0.35, \leq 1.17] \\ t_{28} \in (> 0.40, \leq 1.26] \\ t_{29} \in (> 0.32, \leq 1.26] \\ t_{30} \in (> 0.20, \leq 1.21] \end{cases}$$

$$\hat{y} = "0",$$

$$\Rightarrow \text{CONF}(R_{21}) = 1.00,$$

$$\text{COV}(R_{21}) = 0.02.$$

d) *Union of Anchor + SHAP*

$$R_{21} : \begin{cases} t_4 \in (> -0.92, \leq 0.52] \\ t_5 \in (> -1.36, \leq 0.21] \\ t_6 \in (> -1.69, \leq 0.04] \\ t_{10} \in (> -2.15, \leq -1.13] \\ t_{11} \in (> -2.22, \leq -1.28] \\ t_{22} \in (> 0.15, \leq 0.97] \\ t_{23} \in (> 0.43, \leq 1.23] \\ t_{24} \in (> 0.51, \leq 1.31] \\ t_{25} \in (> 0.51, \leq 1.31] \\ t_{26} \in (> 0.62, \leq 1.41] \\ t_{27} \in (> 0.35, \leq 1.17] \\ t_{28} \in (> 0.40, \leq 1.26] \\ t_{29} \in (> 0.32, \leq 1.26] \\ t_{30} \in (> 0.20, \leq 1.21] \\ t_{42} \leq 0.58 \\ t_{51} \leq 0.23 \end{cases}$$

$$\hat{y} = "0",$$

$$\Rightarrow \text{CONF}(R_{21}) = 1.00,$$

$$\text{COV}(R_{21}) = 0.02.$$

b) LIME (benchmark)

$$R_{21} : \left\{ \begin{array}{l} t_{16} \in (> -2.54, \leq -1.91] \\ t_{17} \in (> -2.63, \leq -2.03] \\ t_{22} \in (> 0.20, \leq 0.93] \\ t_{36} \in (> -0.16, \leq 0.92] \\ t_{37} \in (> -0.29, \leq 0.82] \\ t_{38} \in (> -0.18, \leq 0.97] \\ t_{39} \in (> -0.35, \leq 0.83] \\ t_{40} \in (> -0.32, \leq 0.89] \\ t_{41} \in (> -0.48, \leq 0.76] \\ t_{42} \in (> -0.52, \leq 0.75] \\ t_{43} \in (> -0.51, \leq 0.72] \\ t_{44} \in (> -0.60, \leq 0.56] \\ t_{45} \in (> -0.44, \leq 0.68] \\ t_{46} \in (> -0.55, \leq 0.49] \\ t_{47} \in (> -0.51, \leq 0.46] \\ t_{48} \in (> -0.43, \leq 0.42] \\ t_{49} \in (> -0.37, \leq 0.38] \\ t_{50} \in (> -0.28, \leq 0.40] \\ t_{51} \in (> -0.39, \leq 0.20] \\ t_{52} \in (> -0.36, \leq 0.17] \\ t_{53} \in (> -0.23, \leq 0.25] \\ t_{54} \in (> -0.30, \leq 0.13] \\ t_{55} \in (> -0.18, \leq 0.19] \\ t_{56} \in (> -0.28, \leq 0.08] \\ t_{58} \in (> -0.26, \leq 0.06] \\ t_{59} \in (> -0.15, \leq 0.18] \\ t_{61} \in (> -0.06, \leq 0.23] \\ t_{62} \in (> -0.04, \leq 0.25] \\ t_{63} \in (> -0.09, \leq 0.19] \\ t_{64} \in (> -0.13, \leq 0.13] \\ t_{65} \in (> -0.06, \leq 0.23] \\ t_{66} \in (> -0.19, \leq 0.12] \\ t_{67} \in (> -0.16, \leq 0.17] \\ t_{70} \in (> -0.26, \leq 0.09] \\ t_{71} \in (> -0.26, \leq 0.10] \\ t_{72} \in (> -0.21, \leq 0.18] \end{array} \right.$$

$$\begin{aligned} & \hat{y} = "0", \\ \Rightarrow & \text{CONF}(R_{21}) = 1.00, \\ & \text{COV}(R_{21}) = 0.02. \end{aligned}$$

f) Union of LIME + SHAP

$$R_{21} : \left\{ \begin{array}{l} t_4 \in (> -0.92, \leq 0.52] \\ t_5 \in (> -1.36, \leq 0.21] \\ t_6 \in (> -1.69, \leq 0.04] \\ t_{10} \in (> -2.15, \leq -1.13] \\ t_{11} \in (> -2.22, \leq -1.28] \\ t_{16} \in (> -2.54, \leq -1.91] \\ t_{17} \in (> -2.63, \leq -2.03] \\ t_{22} \in (> 0.15, \leq 0.97] \\ t_{23} \in (> 0.43, \leq 1.23] \\ t_{24} \in (> 0.51, \leq 1.31] \\ t_{25} \in (> 0.51, \leq 1.31] \\ t_{26} \in (> 0.62, \leq 1.41] \\ t_{27} \in (> 0.35, \leq 1.17] \\ t_{28} \in (> 0.40, \leq 1.26] \\ t_{29} \in (> 0.32, \leq 1.26] \\ t_{30} \in (> 0.20, \leq 1.21] \\ t_{36} \in (> -0.16, \leq 0.92] \\ t_{37} \in (> -0.29, \leq 0.82] \\ t_{38} \in (> -0.18, \leq 0.97] \\ t_{39} \in (> -0.35, \leq 0.83] \\ t_{40} \in (> -0.32, \leq 0.89] \\ t_{41} \in (> -0.48, \leq 0.76] \\ t_{42} \in (> -0.52, \leq 0.75] \\ t_{43} \in (> -0.51, \leq 0.72] \\ t_{44} \in (> -0.60, \leq 0.56] \\ t_{45} \in (> -0.44, \leq 0.68] \\ t_{46} \in (> -0.55, \leq 0.49] \\ t_{47} \in (> -0.51, \leq 0.46] \\ t_{48} \in (> -0.43, \leq 0.42] \\ t_{49} \in (> -0.37, \leq 0.38] \\ t_{50} \in (> -0.28, \leq 0.40] \\ t_{51} \in (> -0.39, \leq 0.20] \\ t_{52} \in (> -0.36, \leq 0.17] \\ t_{53} \in (> -0.23, \leq 0.25] \\ t_{54} \in (> -0.30, \leq 0.13] \\ t_{55} \in (> -0.18, \leq 0.19] \\ t_{56} \in (> -0.28, \leq 0.08] \\ t_{58} \in (> -0.26, \leq 0.06] \\ t_{59} \in (> -0.15, \leq 0.18] \\ t_{61} \in (> -0.06, \leq 0.23] \\ t_{62} \in (> -0.04, \leq 0.25] \\ t_{63} \in (> -0.09, \leq 0.19] \\ t_{64} \in (> -0.13, \leq 0.13] \\ t_{65} \in (> -0.06, \leq 0.23] \\ t_{66} \in (> -0.19, \leq 0.12] \\ t_{67} \in (> -0.16, \leq 0.17] \\ t_{70} \in (> -0.26, \leq 0.09] \\ t_{71} \in (> -0.26, \leq 0.10] \\ t_{72} \in (> -0.21, \leq 0.18] \end{array} \right.$$

$$\begin{aligned} & \hat{y} = "0", \\ \Rightarrow & \text{CONF}(R_{21}) = 1.00, \\ & \text{COV}(R_{21}) = 0.02. \end{aligned}$$

g) Best of Anchor + LIME + SHAP

$$R_{21} : \begin{cases} t_{16} \in (> -2.54, \leq -1.91] \\ t_{17} \in (> -2.63, \leq -2.03] \\ t_{22} \in (> 0.20, \leq 0.93] \\ t_{36} \in (> -0.16, \leq 0.92] \\ t_{37} \in (> -0.29, \leq 0.82] \\ t_{38} \in (> -0.18, \leq 0.97] \\ t_{39} \in (> -0.35, \leq 0.83] \\ t_{40} \in (> -0.32, \leq 0.89] \\ t_{41} \in (> -0.48, \leq 0.76] \\ t_{42} \in (> -0.52, \leq 0.75] \\ t_{43} \in (> -0.51, \leq 0.72] \\ t_{44} \in (> -0.60, \leq 0.56] \\ t_{45} \in (> -0.44, \leq 0.68] \\ t_{46} \in (> -0.55, \leq 0.49] \\ t_{47} \in (> -0.51, \leq 0.46] \\ t_{48} \in (> -0.43, \leq 0.42] \\ t_{49} \in (> -0.37, \leq 0.38] \\ t_{50} \in (> -0.28, \leq 0.40] \\ t_{51} \in (> -0.39, \leq 0.20] \\ t_{52} \in (> -0.36, \leq 0.17] \\ t_{53} \in (> -0.23, \leq 0.25] \\ t_{54} \in (> -0.30, \leq 0.13] \\ t_{55} \in (> -0.18, \leq 0.19] \\ t_{56} \in (> -0.28, \leq 0.08] \\ t_{58} \in (> -0.26, \leq 0.06] \\ t_{59} \in (> -0.15, \leq 0.18] \\ t_{61} \in (> -0.06, \leq 0.23] \\ t_{62} \in (> -0.04, \leq 0.25] \\ t_{63} \in (> -0.09, \leq 0.19] \\ t_{64} \in (> -0.13, \leq 0.13] \\ t_{65} \in (> -0.06, \leq 0.23] \\ t_{66} \in (> -0.19, \leq 0.12] \\ t_{67} \in (> -0.16, \leq 0.17] \\ t_{70} \in (> -0.26, \leq 0.09] \\ t_{71} \in (> -0.26, \leq 0.10] \\ t_{72} \in (> -0.21, \leq 0.18] \end{cases}$$

$$\begin{aligned} \hat{y} &= "0", \\ \Rightarrow \text{CONF}(R_{21}) &= 1.00, \\ \text{COV}(R_{21}) &= 0.02. \end{aligned}$$

e) Lasso of LIME + SHAP

$$R_{21} : \begin{cases} t_6 \in (> -1.69, \leq 0.04] \\ t_{11} \in (> -2.22, \leq -1.28] \\ t_{38} \in (> -0.18, \leq 0.97] \\ t_{40} \in (> -0.32, \leq 0.89] \\ t_{41} \in (> -0.48, \leq 0.76] \\ t_{42} \in (> -0.52, \leq 0.75] \\ t_{44} \in (> -0.60, \leq 0.56] \\ t_{46} \in (> -0.55, \leq 0.49] \\ t_{48} \in (> -0.43, \leq 0.42] \\ t_{49} \in (> -0.37, \leq 0.38] \\ t_{51} \in (> -0.39, \leq 0.20] \\ t_{54} \in (> -0.30, \leq 0.13] \\ t_{66} \in (> -0.19, \leq 0.12] \\ t_{67} \in (> -0.16, \leq 0.17] \\ t_{72} \in (> -0.21, \leq 0.18] \end{cases}$$

$$\begin{aligned} \hat{y} &= "0", \\ \Rightarrow \text{CONF}(R_{21}) &= 1.00, \\ \text{COV}(R_{21}) &= 0.02. \end{aligned}$$

h) Lasso of Anchor + LIME + SHAP

$$R_{21} : \begin{cases} t_5 \in (> -1.36, \leq 0.21] \\ t_{11} \in (> -2.22, \leq -1.28] \\ t_{38} \in (> -0.18, \leq 0.97] \\ t_{39} \in (> -0.35, \leq 0.83] \\ t_{40} \in (> -0.32, \leq 0.89] \\ t_{42} \in (> -0.52, \leq 0.75] \\ t_{44} \in (> -0.60, \leq 0.56] \\ t_{46} \in (> -0.55, \leq 0.49] \\ t_{48} \in (> -0.43, \leq 0.42] \\ t_{49} \in (> -0.37, \leq 0.38] \\ t_{51} \leq 0.23 \\ t_{54} \in (> -0.30, \leq 0.13] \\ t_{65} \in (> -0.06, \leq 0.23] \\ t_{67} \in (> -0.16, \leq 0.17] \\ t_{72} \in (> -0.21, \leq 0.18] \end{cases}$$

$$\begin{aligned} \hat{y} &= "0", \\ \Rightarrow \text{CONF}(R_{21}) &= 1.00, \\ \text{COV}(R_{21}) &= 0.02. \end{aligned}$$

4.7.3 Dataset-level visual summary (ECG200 and Plane datasets)

Beyond the single-trace analysis in Sec. 4.7, Appendix A.4 presents a dataset-level visual catalogue for *ECG200* (Appendix A.4.1) and *Plane* (Appendix A.4.2). For each explainer (Anchor, LIME, SHAP) and their fusions (union, lasso, best), we show curated per-class exemplars (diverse instances, prototype, class mean) with the same

red-window overlay used throughout. This complements the pointwise analysis by highlighting recurrent early/mid/late concentrations at the dataset level.

5 Conclusion

This work introduces a novel rule-based explainability framework tailored for *time series (TS)* classification tasks, addressing the current gap in interpretable AI solutions for temporal data. To the best of our knowledge, this is the first systematic study transforming *post-hoc, instance-based numerical feature attributions* from *SHAP* and *LIME* explainers into structured, human-readable rule representations for *TS*. Our approach uniquely integrates and compares these rule-based explanations with *Anchor*, a native rule-based explainer, across a comprehensive benchmark of 43 *TS* datasets from the *UCR/UEA Time Series Classification Archive*. We further contribute a modular *rule fusion* pipeline, combining multiple explainers into a single, optimized rule per instance while ensuring high fidelity and coverage. This work is accompanied by evaluation of multiple rule aggregation strategies, along with an open-source codebase and practical visualization techniques to facilitate adoption in real-world applications.

We transform *numeric feature attribution explainers (LIME, SHAP)* into *rule-based TS explanations*, integrating them with *Anchor*. Our post-hoc framework explains instances post-training, crucial for TS tasks like anomaly detection and decision support (RQ1). *Feature-to-rule conversion* balances complexity, improving *coverage, confidence*, and ensuring interpretability for each instance. Optimizing thresholds and perturbations refines structured, unambiguous rules, improving interpretability. Reliable rules align with model decisions, balancing *confidence* and *coverage* (RQ2).

SHAP and *LIME* perform comparably to *Anchor*, despite the latter being *natively rule-based*. While *Anchor* incurs high computational cost on long *TS*, converting *SHAP* attributions into interval rules provides a more efficient alternative that achieves competitive performance when optimized via *fusion*. Moreover, rules derived from our *numeric-to-rules transformation* use closed intervals $(\ell, u]$ for each timestamp-channel condition, whereas *Anchor* often produces one-sided bounds. Closed intervals are especially important in *TS*, as they precisely delimit both lower and upper thresholds, ensuring that temporal segments are fully specified, reducing ambiguity in sequential explanations, and allowing for clearer visualization.

Our framework consolidates knowledge from multiple explainers (RQ3). Unlike bagging or boosting, our *post-hoc fusion* refines single or multiple explainers into a coherent rule set, aligning with *expert system principles*. *Fusion* improves rule reliability, reduces ambiguity, and enhances decision-making. Moreover, *PHAR* supports *sparsity optimization*. We measure sparsity with the rule-length metric $F(n)$ and report both its mean and median. This is important given human working-memory limits (the 7 ± 2 principle) (Miller 1956), as discussed earlier when defining the objective function. Our method enables this, when desired, by offering resolution modes that promote concise, non-overlapping rules, and by using fusion methods such as

lasso and intersection. This is also illustrated by the ECG200 example discussed in our qualitative evaluation.

Rules enhance *TS* visualization, aiding expert interpretation (RQ4). *Anchor* uses fewer features but produces broad intervals, missing finer temporal details. *SHAP* and *LIME* involve more features, creating narrower, potentially more human-readable intervals that retain predictive alignment while avoiding redundant or overlapping conditions. Application-dependent, broader feature sets or refined intervals enhance explanation resolution.

Interpretability of *fused rules* depends on simplicity (fewer features) and uniqueness (avoiding redundancy), optimized via key metrics. *Rule fusion* removes redundancy, ensuring a structured, coherent set of explanations. Results show that both single-explainer (*SHAP*, *LIME*) and fusion methods achieve high *confidence*, *coverage*, and *explanation ratio*. *Lasso*, *Weighted*, and *Best* refine rules, often improving clarity and consistency, while visualization enhances the illustration of rule applicability.

5.1 Limitations

The *PHAR* framework effectively transforms numeric feature attributions into rule-based explanations, but several limitations remain.

1. Rule quality within *PHAR* depends on explainers such as *SHAP* and *LIME*, which rely on perturbation-based sampling and may produce unstable attributions, particularly in noisy or highly dynamic time series.
2. Computational complexity represents a secondary limitation; while the transformation step in *PHAR* involves hyperparameter tuning, we have shown in Section 4.2 that the practical cost remains acceptable due to parallelization, the optional nature of tuning, and the complexity of the `fusion` step, with the exception of the more computationally intensive `Lasso global` variant.
3. Our evaluation of *PHAR* employed a predefined set of metrics, and further exploration of alternative rule selection criteria could enhance the flexibility of rule generation.
4. Interpretability within *PHAR* may be challenged in high-dimensional time series, where resulting rules risk becoming overly specific; however, this issue is partially mitigated by the dedicated visualization techniques developed in *PHAR*, which follow a semifactual design and aim to present rule intervals in a clearer, more interpretable manner. Future work could further address this limitation by incorporating feature selection mechanisms or additional constraints to promote more generalizable rule representations.
5. While our visualization experiments within *PHAR* demonstrated practical applicability, we did not conduct evaluations with *Domain Experts*, and the relationship between rule complexity and perceived clarity remains to be systematically investigated.
6. Finally, although `fusion` in *PHAR* balances rule importance, it does not fully eliminate potential conflicts between different explainers. Additionally, we did not explicitly analyze rule similarity or stability, which could be particularly relevant in time series contexts where neighboring time steps may influence model predictions in a correlated manner.

5.2 Future work

While our framework effectively transforms numeric feature attributions into rule-based explanations, several directions remain open.

1. One of the important directions is extending *PHAR* to *counterfactual explanation* generation, by identifying and presenting the nearest time series belonging to an alternative class. This would allow *Domain Experts* to specify transitions from the current predicted class to any arbitrary target class (e.g., in predictive maintenance or clinical decision support), thereby providing actionable "*WHAT-IF*" insights.
2. Further research should assess rule stability across similar instances, determining whether minor input variations lead to consistent explanations.
3. Integrating expert feedback could refine rule usability, bridging automated rule extraction with human interpretability. One approach is incorporating symbolic reasoning systems like *HeaRTDroid* (Bobek et al. 2019)⁹, a lightweight rule engine for expert systems, enabling a hybrid approach that merges statistical learning with structured decision-making.
4. For improvement of interpretability, it will be worth investigating the trade-off between feature count and interval width.
5. Usage of advanced visualization methods, such as interactive overlays or multi-dimensional interval representations could be beneficial. Related direction is *DeepVATS* (Rodriguez-Fernandez et al. 2023)¹⁰, which integrates DL with interactive visualization of latent space projections for *TS*, similar to *TensorFlow Embeddings Projector*, aiding in anomaly detection and structure analysis.
6. Finally, expanding the framework beyond *TS classification* to areas like sequential decision-making or tabular datasets with temporal dependencies could validate its broader applicability.

Supplementary information. Additional tables supporting the statistical comparison of rule-based explainers and fusion methods via Critical Difference Diagrams are provided in "Supplementary Materials" (Section B).

Acknowledgements. This paper is part of a project that has received funding from the European Union's Horizon Europe Research and Innovation Programme under Grant Agreement No. 101120406. The paper reflects only the authors' view and the European Commission is not responsible for any use that may be made of the information contained herein.

Contribution of Maciej Mozolewski for the research for this publication has been supported by a grant from the Priority Research Area (DigiWorld) under the Mark Kac Center for Complex Systems Research Strategic Programme Excellence Initiative at Jagiellonian University.

We thank all contributors of open-source libraries (e.g., TensorFlow, Optuna) and the maintainers of the *UCR/UEA Time Series Classification Archive* for curating

⁹<https://heartdroid.re/>

¹⁰<https://github.com/vrodriguezf/deepvats>

and providing the datasets. We used OpenAI’s GPT to assist in writing and refining the text and generating code snippets, while all conceptual ideas and research contributions were developed by the authors.

References

- Arshad, S., Latif, S., Salman, A., Latif, R.: Enhancing profitability and investor confidence through interpretable ai models for investment decisions. *Journal of Financial AI Research* (2024). Preprint available at [arXiv:2312.16223v2](https://arxiv.org/abs/2312.16223v2)
- Akiba, T., Sano, S., Yanase, T., Ohta, T., Koyama, M.: Optuna: A next-generation hyperparameter optimization framework. In: *Proceedings of the 25th ACM SIGKDD International Conference on Knowledge Discovery and Data Mining* (2019)
- Altmann, A., Tolosi, L., Sander, O., Lengauer, T.: Permutation importance: A corrected feature importance measure. *Bioinformatics* (Oxford, England) **26**, 1340–1347 (2010)
- Arsenault, P.-D., Wang, S., Patenaude, J.-M.: A Survey of Explainable Artificial Intelligence (XAI) in Financial Time Series Forecasting (2024)
- Bach, S., Binder, A., Montavon, G., Klauschen, F., Müller, K.-R., Samek, W.: On pixel-wise explanations for non-linear classifier decisions by layer-wise relevance propagation. *PloS ONE* **10**(7), 0130140 (2015)
- Bagnall, A., Dau, H.A., Lines, J., Flynn, M., Large, J., Bostrom, A., Southam, P., Keogh, E.: The UEA multivariate time series classification archive, 2018 (2018). <https://arxiv.org/abs/1811.00075>
- Bobek, S., Nalepa, G.J.: Tsproto: Fusing deep feature extraction with interpretable glass-box surrogate model for explainable time-series classification. *Information Fusion* **124**, 103357 (2025) <https://doi.org/10.1016/j.inffus.2025.103357>
- Bobek, S., Nalepa, G.J., Ślażyński, M.: Heartdroid—rule engine for mobile and context-aware expert systems. *Expert Systems* **36**(1), 12328 (2019). e12328 [10.1111/exsy.12328](https://doi.org/10.1111/exsy.12328)
- Dau, H.A., Bagnall, A., Kamgar, K., Yeh, C.-C.M., Zhu, Y., Gharghabi, S., Ratanamahatana, C.A., Keogh, E.: The ucr time series archive. *IEEE/CAA Journal of Automatica Sinica* **6**(6), 1293–1305 (2019) <https://doi.org/10.1109/JAS.2019.1911747>
- Davis, R., Buchanan, B., Shortliffe, E.: Production rules as a representation for a knowledge-based consultation program. *Artificial Intelligence* **8**(1), 15–45 (1977) [https://doi.org/10.1016/0004-3702\(77\)90003-0](https://doi.org/10.1016/0004-3702(77)90003-0)

- Dietterich, T.G.: Ensemble methods in machine learning. In: Proceedings of the First International Workshop on Multiple Classifier Systems (MCS 2000). Lecture Notes in Computer Science, vol. 1857, pp. 1–15. Springer, Berlin, Heidelberg (2000)
- Gu, X., Yang, L., Sun, L.: Explainable Artificial Intelligence for Time Series: A Systematic Survey. https://www.researchgate.net/publication/381733392_Explainable_Artificial_Intelligence_for_Time_Series_A_Systematic_Survey. Preprint; accessed Jul 2025 (2024)
- Hryniewska-Guzik, W., Sawicki, B., Biecek, P.: NormEnsembleXAI: Unveiling the Strengths and Weaknesses of XAI Ensemble Techniques (2024). <https://doi.org/10.48550/arXiv.2401.17200> . <https://arxiv.org/pdf/2401.17200>
- Jeyakumar, J.V., Noor, J., Cheng, Y.-H., Garcia, L., Srivastava, M.: How can i explain this to you? an empirical study of deep neural network explanation methods. In: Advances in Neural Information Processing Systems. Advances in Neural Information Processing Systems, vol. 33, pp. 4211–4222. Curran Associates, Inc., Red Hook, NY (2020)
- Jin, D., Sergeeva, E., Weng, W.-H., Chauhan, G., Szolovits, P.: Explainable deep learning in healthcare: A methodological survey from an attribution view. *Advanced Review in AI and Healthcare* (2021). Preprint available at arXiv:2112.02625v1
- Ligeża, A.: Logical Foundations for Rule-Based Systems, 2nd edn. Studies in Computational Intelligence, vol. 11, pp. –1309. Springer, Berlin, Heidelberg (2006)
- Lundberg, S., Lee, S.-I.: A Unified Approach to Interpreting Model Predictions (2017)
- Moreira, C., Chou, Y.-L., Velmurugan, M., Ouyang, C., Sindhgatta, R., Bruza, P.: Linda-bn: An interpretable probabilistic approach for demystifying black-box predictive models. *Decision Support Systems* **150**, 113561 (2021)
- Miller, G.A.: The magical number seven, plus or minus two: Some limits on our capacity for processing information. *Psychological Review* **63**(2), 81–97 (1956) <https://doi.org/10.1037/h0043158>
- Macha, D., Kozielski, M., Wróbel, Sikora, M.: Rulexai—a package for rule-based explanations of machine learning model. *SoftwareX* **20**, 101209 (2022)
- Mekonnen, E.T., Longo, L., Dondio, P.: A global model-agnostic rule-based xai method based on parameterized event primitives for time series classifiers. *Frontiers in Artificial Intelligence* **7** (2024)
- Nalepa, G.J.: In: Gawęda, A.E., Kacprzyk, J., Rutkowski, L., Yen, G.G. (eds.) *Techniques for Construction and Integration of Rule Bases*, pp. 203–223. Springer, Cham (2018)

- Nimmy, S.F., Hussain, O.K., Chakraborty, R.K., Hussain, F.K., Saberi, M.: An optimized belief-rule-based (brb) approach to ensure the trustworthiness of interpreted time-series decisions. *Knowledge-based systems* **271**, 110552 (2023)
- Niederliński, A.: *Regułowo-modelowe Systemy Ekspertowe: Rmse, 2 poprawione, rozszerzone i uściślone edn.* Wydawnictwo Pracowni Komputerowej Jacka Skalmierskiego, Gliwice (2013). <http://www.rmse.pl>
- Rajapaksha, D., Bergmeir, C.: LIMREF: Local Interpretable Model Agnostic Rule-based Explanations for Forecasting, with an Application to Electricity Smart Meter Data (2022)
- Rodriguez-Fernandez, V., Montalvo-Garcia, D., Piccialli, F., Nalepa, G.J., Camacho, D.: Deepvats: Deep visual analytics for time series. *Knowledge-Based Systems* **277**, 110793 (2023)
- Rojat, T., Puget, R., Filliat, D., Del Ser, J., Gelin, R., Díaz-Rodríguez, N.: Explainable artificial intelligence (xai) on timeseries data: a survey. *arXiv preprint arXiv:2104.00950* (2021)
- Ribeiro, M.T., Singh, S., Guestrin, C.: "why should i trust you?": Explaining the predictions of any classifier. In: *Proceedings of the 22nd ACM SIGKDD International Conference on Knowledge Discovery and Data Mining. KDD '16*, pp. 1135–1144. Association for Computing Machinery, New York, NY, USA (2016). <https://doi.org/10.1145/2939672.2939778> . <https://doi.org/10.1145/2939672.2939778>
- Ribeiro, M.T., Singh, S., Guestrin, C.: Anchors: High-precision model-agnostic explanations. *Proceedings of the AAAI Conference on Artificial Intelligence* **32**(1) (2018) <https://doi.org/10.1609/aaai.v32i1.11491>
- Schlegel, U., Arnout, H., El-Assady, M., Oelke, D., Keim, D.A.: Towards a rigorous evaluation of xai methods on time series. *2019 IEEE/CVF International Conference on Computer Vision Workshop (ICCVW)*, 4197–4201 (2019)
- Silva, R.R.C., Caminhas, W.M., De Lima E Silva, P.C.L., Guimaraes, F.G.: A c4.5 fuzzy decision tree method for multivariate time series forecasting. In: *IEEE International Conference on Fuzzy Systems (FUZZ-IEEE)*, vol. 2021-July, pp. 1–6. Institute of Electrical and Electronics Engineers Inc., Luxembourg, Luxembourg (2021)
- Spinnato, F., Guidotti, R., Monreale, A., Nanni, M., Pedreschi, D., Giannotti, F.: Understanding any time series classifier with a subsequence-based explainer. *ACM transactions on knowledge discovery from data* **18**(2), 1–34 (2023)
- Simonyan, K., Vedaldi, A., Zisserman, A.: Deep inside convolutional networks: Visualising image classification models and saliency maps. *arXiv preprint arXiv:1312.6034* (2013)

- Skulmowski, A., Xu, K.M.: Understanding cognitive load in digital and online learning: a new perspective on extraneous cognitive load. *Educational Psychology Review* **34**(1), 171–196 (2022) <https://doi.org/10.1007/s10648-021-09624-7>
- Terpilowski, M.: scikit-posthocs: Pairwise multiple comparison tests in python. *The Journal of Open Source Software* **4**(36), 1169 (2019)
- Tibshirani, R.: Regression shrinkage and selection via the lasso. *Journal of the Royal Statistical Society. Series B (Methodological)* **58**(1), 267–288 (1996). Accessed 2025-07-16
- Theissler, A., Spinnato, F., Schlegel, U., Guidotti, R.: Explainable ai for time series classification: A review, taxonomy and research directions. *IEEE Access* **10**, 100700–100724 (2022) <https://doi.org/10.1109/ACCESS.2022.3207765>
- Veerappa, M., Anneken, M., Burkart, N.: Evaluation of interpretable association rule mining methods on time-series in the maritime domain. In: *Pattern Recognition. ICPR International Workshops and Challenges: Virtual Event, January 10–15, 2021, Proceedings, Part III*, pp. 204–218. Springer, Berlin, Heidelberg (2021)
- Webb, G.I.: Discovering associations with numeric variables. In: *Proceedings of the Seventh ACM SIGKDD International Conference on Knowledge Discovery and Data Mining. KDD '01*, pp. 383–388. Association for Computing Machinery, New York, NY, USA (2001)
- Xie, C., Rajan, D., Chai, Q.: An interpretable neural fuzzy hammerstein-wiener network for stock price prediction. *Information Sciences* **577**, 324–335 (2021)

Appendix A

A.1 Additional Tables

A.1.1 Hyperparameter for Numeric-to-Rules Transformation

Table A1 Hyperparameter Ranges for Optimization

Hyperparam.	Range/Values	Description
p	50 to 99 (step=1)	Percentile for determining feature importance thresholds.
δ	{True, False}	Global vs. per-feature threshold application.
σ_p	0.01 to 1.0 (continuous)	Scale of perturbation for interval estimation.
N_p	1,000 to 10,000 (step=1,000)	Number of perturbed samples for interval estimation and confidence evaluation.

p - threshold percentile, δ - global importance indicator, σ_p - perturbation scale, N_p - perturbation samples count

A.1.2 Experimental Time Series, Explainers and Fused Rule Sets

Dataset	Type	Acc	#F	Dim	#B	#E	Methods					Baselines			Fused rule sets		
							Best	Union	Lasso global	Lasso	Weighted	Intersection	Anchor	SHAP	LIME	Anchor + SHAP	Anchor + LIME
ArticularyWordRecognition	m	96.53	1296	144 × 9	2	12	✓	✓	✓	✓	✓	✓	✓	✓	✓	✓	✓
AtrialFibrillation	m	37.50	1280	640 × 2	2	12	✓	✓	✓	✓	✓	✓	✓	✓	✓	✓	✓
BasicMotions	m	100.00	600	100 × 6	2	12	✓	✓	✓	✓	✓	✓	✓	✓	✓	✓	✓
Cricket	m	93.33	7182	1197 × 6	2	12	✓	✓	✓	✓	✓	✓	✓	✓	✓	✓	✓
ERing	m	98.67	260	65 × 4	2	12	✓	✓	✓	✓	✓	✓	✓	✓	✓	✓	✓
Epilepsy	m	91.30	618	206 × 3	2	12	✓	✓	✓	✓	✓	✓	✓	✓	✓	✓	✓
Libras	m	63.33	90	45 × 2	1	3	✓	✓	✓	✓	✓	✓	✓	✓	✓	✓	✓
PenDigits	m	99.24	16	8 × 2	1	3	✓	✓	✓	✓	✓	✓	✓	✓	✓	✓	✓
Adiac	u	29.59	176	176 × 1	2	12	✓	✓	✓	✓	✓	✓	✓	✓	✓	✓	✓
BME	u	86.67	128	128 × 1	2	12	✓	✓	✓	✓	✓	✓	✓	✓	✓	✓	✓
Beef	u	53.33	470	470 × 1	2	12	✓	✓	✓	✓	✓	✓	✓	✓	✓	✓	✓
BeetleFly	u	80.00	512	512 × 1	2	12	✓	✓	✓	✓	✓	✓	✓	✓	✓	✓	✓
BirdChicken	u	50.00	512	512 × 1	2	12	✓	✓	✓	✓	✓	✓	✓	✓	✓	✓	✓
CBF	u	100.00	128	128 × 1	2	12	✓	✓	✓	✓	✓	✓	✓	✓	✓	✓	✓
Chinatown	u	98.90	24	24 × 1	3	33	✓	✓	✓	✓	✓	✓	✓	✓	✓	✓	✓
CricketX	u	61.54	300	300 × 1	1	3	✓	✓	✓	✓	✓	✓	✓	✓	✓	✓	✓
DiatomSizeReduction	u	100.00	345	345 × 1	2	12	✓	✓	✓	✓	✓	✓	✓	✓	✓	✓	✓
DistalPhalanxOutlineAgeGroup	u	77.78	80	80 × 1	1	3	✓	✓	✓	✓	✓	✓	✓	✓	✓	✓	✓
DistalPhalanxOutlineCorrect	u	78.08	80	80 × 1	1	3	✓	✓	✓	✓	✓	✓	✓	✓	✓	✓	✓
DodgerLoopDay	u	55.00	288	288 × 1	3	33	✓	✓	✓	✓	✓	✓	✓	✓	✓	✓	✓
DodgerLoopGame	u	87.50	288	288 × 1	3	33	✓	✓	✓	✓	✓	✓	✓	✓	✓	✓	✓
EKG200	u	86.00	96	96 × 1	3	33	✓	✓	✓	✓	✓	✓	✓	✓	✓	✓	✓
ECG5000	u	91.52	140	140 × 1	1	3	✓	✓	✓	✓	✓	✓	✓	✓	✓	✓	✓
ECGFiveDays	u	100.00	136	136 × 1	3	33	✓	✓	✓	✓	✓	✓	✓	✓	✓	✓	✓
FaceFour	u	96.43	350	350 × 1	1	3	✓	✓	✓	✓	✓	✓	✓	✓	✓	✓	✓
GunPoint	u	86.00	150	150 × 1	2	12	✓	✓	✓	✓	✓	✓	✓	✓	✓	✓	✓
GunPointAgeSpan	u	88.50	150	150 × 1	3	33	✓	✓	✓	✓	✓	✓	✓	✓	✓	✓	✓
GunPointMaleVersusFemale	u	100.00	150	150 × 1	2	12	✓	✓	✓	✓	✓	✓	✓	✓	✓	✓	✓
GunPointOldVersusYoung	u	100.00	150	150 × 1	2	12	✓	✓	✓	✓	✓	✓	✓	✓	✓	✓	✓
InsectWingbeatSound	u	66.91	256	256 × 1	1	3	✓	✓	✓	✓	✓	✓	✓	✓	✓	✓	✓
MedicalImages	u	68.53	99	99 × 1	1	3	✓	✓	✓	✓	✓	✓	✓	✓	✓	✓	✓
MiddlePhalanxOutlineAgeGroup	u	78.42	80	80 × 1	1	3	✓	✓	✓	✓	✓	✓	✓	✓	✓	✓	✓
PhalangesOutlinesCorrect	u	67.07	80	80 × 1	1	3	✓	✓	✓	✓	✓	✓	✓	✓	✓	✓	✓
Plane	u	96.23	144	144 × 1	3	33	✓	✓	✓	✓	✓	✓	✓	✓	✓	✓	✓
PowerCons	u	100.00	144	144 × 1	1	3	✓	✓	✓	✓	✓	✓	✓	✓	✓	✓	✓
ProximalPhalanxTW	u	48.68	80	80 × 1	3	33	✓	✓	✓	✓	✓	✓	✓	✓	✓	✓	✓
SmoothSubspace	u	96.00	15	15 × 1	1	3	✓	✓	✓	✓	✓	✓	✓	✓	✓	✓	✓
Strawberry	u	77.64	235	235 × 1	1	3	✓	✓	✓	✓	✓	✓	✓	✓	✓	✓	✓
SyntheticControl	u	89.33	60	60 × 1	1	3	✓	✓	✓	✓	✓	✓	✓	✓	✓	✓	✓
Trace	u	68.00	275	275 × 1	1	3	✓	✓	✓	✓	✓	✓	✓	✓	✓	✓	✓
TwoPatterns	u	99.92	128	128 × 1	2	12	✓	✓	✓	✓	✓	✓	✓	✓	✓	✓	✓
UMD	u	93.33	150	150 × 1	3	33	✓	✓	✓	✓	✓	✓	✓	✓	✓	✓	✓
Wafer	u	99.83	152	152 × 1	3	33	✓	✓	✓	✓	✓	✓	✓	✓	✓	✓	✓

Table A.2 Dataset summary with baselines, methods, and fusion methods. **Type** is represented as **u** (univariate) or **m** (multivariate). Column **Acc** denotes Accuracy of the ML model. Column **#F** denotes the total number of input features, and **Dim** denotes the input time series dimensionality (time × variables). Columns **#B** and **#E** indicate the number of baselines and ensembles for each dataset.

A.1.3 Wilcoxon Signed-rank Tests

Table A3 Wilcoxon signed-rank test results comparing baselines (single explainers: Anchor, LIME, SHAP) for each metric. Columns include medians for each pair, test statistic (W), p-value (p), and the number of compared pairs (N). Statistically significant results are marked with asterisks: * ($p < 0.05$), ** ($p < 0.01$), *** ($p < 0.001$).

Metric	Explainers	N	Median1	Median2	W	p
\bar{M}	Anchor vs LIME	10	16.89	4.95	2.0	0.006**
	Anchor vs SHAP	10	16.89	6.86	4.0	0.014*
	LIME vs SHAP	27	3.30	2.56	177.0	0.79
$C\bar{O}N\bar{F} \cdot ER$	Anchor vs LIME	10	83.43	65.75	20.0	0.49
	Anchor vs SHAP	10	83.43	86.99	24.0	0.77
	LIME vs SHAP	27	63.70	89.17	55.0	< 0.001***
$C\bar{O}N\bar{F} \cdot C\bar{O}V \cdot ER$	Anchor vs LIME	10	17.48	6.03	5.0	0.019*
	Anchor vs SHAP	10	17.48	7.82	6.0	0.027*
	LIME vs SHAP	27	7.83	6.24	154.0	0.41
$C\bar{O}N\bar{F}$	Anchor vs LIME	10	0.88	0.88	16.0	0.28
	Anchor vs SHAP	10	0.88	0.94	24.0	0.77
	LIME vs SHAP	27	0.82	0.92	60.0	0.001**
$C\bar{O}V$	Anchor vs LIME	10	0.20	0.12	12.0	0.13
	Anchor vs SHAP	10	0.20	0.09	11.0	0.11
	LIME vs SHAP	27	0.13	0.10	113.0	0.07
ER	Anchor vs LIME	10	98.03	88.10	17.0	0.89
	Anchor vs SHAP	10	98.03	100.00	10.0	0.92
	LIME vs SHAP	27	86.11	100.00	62.0	0.06
$F(\bar{n})$	Anchor vs LIME	10	1.94	13.46	1.0	0.004**
	Anchor vs SHAP	10	1.94	7.12	1.0	0.004**
	LIME vs SHAP	27	19.98	32.04	137.0	0.22
$Med(F(n))$	Anchor vs LIME	10	2.00	8.00	4.0	0.014*
	Anchor vs SHAP	10	2.00	6.50	1.5	0.013*
	LIME vs SHAP	27	9.50	21.00	89.0	0.048*

Table A4 Wilcoxon signed-rank test results comparing explainers (and their fused rule sets) to Anchor (Baseline) for \bar{M} .

Explainers set	N	Median ₁	Median ₂	W	p
Anchor+LIME vs Anchor	10	9.94	17.29	0.00	0.002**
Anchor+LIME+SHAP vs Anchor	10	7.60	17.29	3.00	0.010**
Anchor+SHAP vs Anchor	10	11.03	17.29	5.00	0.019*
LIME vs Anchor	10	4.65	17.29	0.00	0.002**
LIME+SHAP vs Anchor	10	5.79	17.29	0.00	0.002**
SHAP vs Anchor	10	8.32	17.29	0.00	0.002**
*p(<0.05), **p(<0.01), ***p(<0.001)					

Table A5 Wilcoxon signed-rank test results comparing explainers (and their fused rule sets) to Anchor (Baseline) for $\overline{CONF} \cdot ER$.

Explainers set	N	Median ₁	Median ₂	W	p
Anchor+LIME vs Anchor	10	74.08	68.71	20.00	0.49
Anchor+LIME+SHAP vs Anchor	10	69.32	68.71	27.00	1.00
Anchor+SHAP vs Anchor	10	77.28	68.71	15.00	0.23
LIME vs Anchor	10	59.68	68.71	15.00	0.23
LIME+SHAP vs Anchor	10	73.12	68.71	26.00	0.92
SHAP vs Anchor	10	70.64	68.71	21.00	0.56
*p(<0.05), **p(<0.01), ***p(<0.001)					

Table A6 Wilcoxon signed-rank test results comparing explainers (and their fused rule sets) to Anchor (Baseline) for $\overline{CONF} \cdot \overline{COV} \cdot ER$.

Explainers set	N	Median ₁	Median ₂	W	p
Anchor+LIME vs Anchor	10	11.36	18.64	4.00	0.014*
Anchor+LIME+SHAP vs Anchor	10	9.02	18.64	4.00	0.014*
Anchor+SHAP vs Anchor	10	11.86	18.64	5.00	0.019*
LIME vs Anchor	10	5.87	18.64	2.00	0.006**
LIME+SHAP vs Anchor	10	7.14	18.64	1.00	0.004**
SHAP vs Anchor	10	8.85	18.64	0.00	0.002**
*p(<0.05), **p(<0.01), ***p(<0.001)					

Table A7 Wilcoxon signed-rank test results comparing explainers (and their fused rule sets) to Anchor (Baseline) for \overline{CONF} .

Explainers set	N	Median ₁	Median ₂	W	p
Anchor+LIME vs Anchor	10	0.85	0.84	17.00	0.32
Anchor+LIME+SHAP vs Anchor	10	0.87	0.84	9.00	0.06
Anchor+SHAP vs Anchor	10	0.88	0.84	4.00	0.014*
LIME vs Anchor	10	0.81	0.84	13.00	0.16
LIME+SHAP vs Anchor	10	0.89	0.84	20.00	0.49
SHAP vs Anchor	10	0.86	0.84	26.00	0.92
*p(<0.05), **p(<0.01), ***p(<0.001)					

Table A8 Wilcoxon signed-rank test results comparing explainers (and their fused rule sets) to Anchor (Baseline) for $C\bar{O}V$.

Explainers set	N	Median ₁	Median ₂	W	p
Anchor+LIME vs Anchor	10	0.19	0.26	1.00	0.004**
Anchor+LIME+SHAP vs Anchor	10	0.15	0.26	1.00	0.004**
Anchor+SHAP vs Anchor	10	0.19	0.26	2.00	0.006**
LIME vs Anchor	10	0.15	0.26	9.00	0.06
LIME+SHAP vs Anchor	10	0.12	0.26	6.00	0.027*
SHAP vs Anchor	10	0.16	0.26	8.00	0.049*
*p(<0.05), **p(<0.01), ***p(<0.001)					

Table A9 Wilcoxon signed-rank test results comparing explainers (and their fused rule sets) to Anchor (Baseline) for ER .

Explainers set	N	Median ₁	Median ₂	W	p
Anchor+LIME vs Anchor	10	81.37	89.87	27.00	1.00
Anchor+LIME+SHAP vs Anchor	10	79.71	89.87	19.00	0.43
Anchor+SHAP vs Anchor	10	87.25	89.87	22.00	0.62
LIME vs Anchor	10	70.55	89.87	16.00	0.28
LIME+SHAP vs Anchor	10	81.04	89.87	24.00	0.77
SHAP vs Anchor	10	76.81	89.87	15.00	0.23
*p(<0.05), **p(<0.01), ***p(<0.001)					

Table A10 Wilcoxon signed-rank test results comparing explainers (and their fused rule sets) to Anchor (Baseline) for $F(\bar{n})$.

Explainers set	N	Median ₁	Median ₂	W	p
Anchor+LIME vs Anchor	10	7.34	1.55	0.00	0.002**
Anchor+LIME+SHAP vs Anchor	10	9.89	1.55	1.00	0.004**
Anchor+SHAP vs Anchor	10	4.56	1.55	1.00	0.004**
LIME vs Anchor	10	9.12	1.55	1.00	0.004**
LIME+SHAP vs Anchor	10	12.24	1.55	1.00	0.004**
SHAP vs Anchor	10	4.18	1.55	2.00	0.006**
*p(<0.05), **p(<0.01), ***p(<0.001)					

Table A11 Wilcoxon signed-rank test results comparing explainers (and their fused rule sets) to Anchor (Baseline) for $Med(F(n))$.

Explainers set	N	Median ₁	Median ₂	W	p
Anchor+LIME vs Anchor	10	3.29	1.75	0.00	0.002**
Anchor+LIME+SHAP vs Anchor	10	5.96	1.75	1.00	0.004**
Anchor+SHAP vs Anchor	10	2.92	1.75	1.00	0.004**
LIME vs Anchor	10	4.50	1.75	4.00	0.014*
LIME+SHAP vs Anchor	10	8.50	1.75	1.00	0.004**
SHAP vs Anchor	10	3.88	1.75	5.50	0.027*
*p(<0.05), **p(<0.01), ***p(<0.001)					

Table A12 Wilcoxon signed-rank test results comparing fusion methods (consisting of one or more explainers) to the Baseline explainer (Anchor, LIME or SHAP) for \bar{M} .

Methods	N	Median ₁	Median ₂	W	p
Best vs Baseline	27	5.57	5.46	163.00	0.55
Intersection vs Baseline	27	3.92	5.46	166.00	0.59
Lasso vs Baseline	40	7.56	5.66	146.00	< 0.001***
Lasso global vs Baseline	43	6.92	5.40	377.00	0.25
Union vs Baseline	27	1.76	5.46	48.00	< 0.001***
Weighted vs Baseline	27	6.29	5.46	82.00	0.009**

*p(<0.05), **p(<0.01), ***p(<0.001)

Table A13 Wilcoxon signed-rank test results comparing fusion methods (consisting of one or more explainers) to the Baseline explainer (Anchor, LIME or SHAP) for $\overline{CONF} \cdot ER$.

Methods	N	Median ₁	Median ₂	W	p
Best vs Baseline	27	95.59	70.97	0.00	< 0.001***
Intersection vs Baseline	27	50.46	70.97	62.00	0.002**
Lasso vs Baseline	40	78.49	73.31	114.00	< 0.001***
Lasso global vs Baseline	43	28.73	70.97	141.00	< 0.001***
Union vs Baseline	27	94.21	70.97	9.00	< 0.001***
Weighted vs Baseline	27	76.89	70.97	79.00	0.007**

*p(<0.05), **p(<0.01), ***p(<0.001)

Table A14 Wilcoxon signed-rank test results comparing fusion methods (consisting of one or more explainers) to the Baseline explainer (Anchor, LIME or SHAP) for $\overline{CONF} \cdot \overline{COV} \cdot ER$.

Methods	N	Median ₁	Median ₂	W	p
Best vs Baseline	27	10.00	11.26	152.00	0.39
Intersection vs Baseline	27	6.93	11.26	105.00	0.044*
Lasso vs Baseline	40	10.38	11.02	245.00	0.026*
Lasso global vs Baseline	43	9.85	10.02	459.00	0.87
Union vs Baseline	27	5.64	11.26	82.00	0.009**
Weighted vs Baseline	28	12.15	11.31	95.00	0.013*

*p(<0.05), **p(<0.01), ***p(<0.001)

Table A15 Wilcoxon signed-rank test results comparing fusion methods (consisting of one or more explainers) to the Baseline explainer (Anchor, LIME or SHAP) for *CONF*.

Methods	N	Median ₁	Median ₂	W	p
Best vs Baseline	27	0.97	0.85	0.00	< 0.001***
Intersection vs Baseline	27	0.83	0.85	85.00	0.011*
Lasso vs Baseline	40	0.88	0.84	178.00	0.001**
Lasso global vs Baseline	43	0.68	0.85	72.00	< 0.001***
Union vs Baseline	27	0.94	0.85	47.00	< 0.001***
Weighted vs Baseline	27	0.88	0.85	41.00	< 0.001***

*p(<0.05), **p(<0.01), ***p(<0.001)

Table A16 Wilcoxon signed-rank test results comparing fusion methods (consisting of one or more explainers) to the Baseline explainer (Anchor, LIME or SHAP) for *COV*.

Methods	N	Median ₁	Median ₂	W	p
Best vs Baseline	27	0.11	0.17	38.00	< 0.001***
Intersection vs Baseline	27	0.16	0.17	178.00	0.80
Lasso vs Baseline	40	0.17	0.18	395.00	0.85
Lasso global vs Baseline	42	0.34	0.19	2.00	< 0.001***
Union vs Baseline	27	0.06	0.17	16.00	< 0.001***
Weighted vs Baseline	27	0.17	0.17	172.00	0.70

*p(<0.05), **p(<0.01), ***p(<0.001)

Table A17 Wilcoxon signed-rank test results comparing fusion methods (consisting of one or more explainers) to the Baseline explainer (Anchor, LIME or SHAP) for *ER*.

Methods	N	Median ₁	Median ₂	W	p
Best vs Baseline	21	100.00	86.67	0.00	< 0.001***
Intersection vs Baseline	27	70.00	90.00	65.00	0.002**
Lasso vs Baseline	25	93.02	90.00	26.00	< 0.001***
Lasso global vs Baseline	43	53.43	91.67	241.00	0.004**
Union vs Baseline	21	100.00	86.67	0.00	< 0.001***
Weighted vs Baseline	26	89.60	90.39	148.00	0.50

*p(<0.05), **p(<0.01), ***p(<0.001)

Table A18 Wilcoxon signed-rank test results comparing fusion methods (consisting of one or more explainers) to the Baseline explainer (Anchor, LIME or SHAP) for $F(\bar{n})$.

Methods	N	Median ₁	Median ₂	W	p
Best vs Baseline	27	27.50	23.59	90.00	0.016*
Intersection vs Baseline	27	6.07	23.59	40.00	< 0.001***
Lasso vs Baseline	40	5.05	10.65	19.00	< 0.001***
Lasso global vs Baseline	43	1.02	9.33	46.00	< 0.001***
Union vs Baseline	27	42.61	23.59	0.00	< 0.001***
Weighted vs Baseline	27	23.90	23.59	128.00	0.15

*p(<0.05), **p(<0.01), ***p(<0.001)

Table A19 Wilcoxon signed-rank test results comparing fusion methods (consisting of one or more explainers) to the Baseline explainer (Anchor, LIME or SHAP) for $Med(F(n))$.

Methods	N	Median ₁	Median ₂	W	p
Best vs Baseline	26	26.50	21.58	61.50	0.003**
Intersection vs Baseline	27	2.25	20.50	34.00	< 0.001***
Lasso vs Baseline	28	4.83	21.58	44.00	< 0.001***
Lasso global vs Baseline	42	0.67	7.17	73.00	< 0.001***
Union vs Baseline	27	42.00	20.50	0.00	< 0.001***
Weighted vs Baseline	26	17.33	21.58	132.50	0.28

*p(<0.05), **p(<0.01), ***p(<0.001)

A.1.4 Median Values of Metrics

Table A20 Summary of medians for fusion combinations across all metrics.

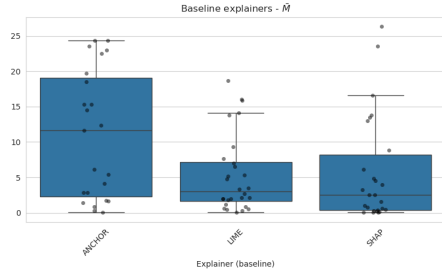
Fusion	N	\bar{M}	$C\bar{O}N\bar{F} \cdot ER$	$C\bar{O}N\bar{F} \cdot C\bar{O}V \cdot ER$	$C\bar{O}N\bar{F}$	$C\bar{O}V$	ER	$F(\bar{n})$	$Med(F(\bar{n}))$
Anchor	100	17.24	79.81	17.86	0.87	0.22	97.03	1.79	2.00
Anchor+LIME	60	10.62	84.73	12.31	0.90	0.17	95.92	6.66	2.75
Anchor+SHAP	60	10.44	90.47	12.01	0.92	0.15	97.69	4.91	2.25
Anchor+LIME+SHAP	60	6.92	84.52	8.55	0.91	0.12	93.59	8.49	4.75
SHAP	108	6.86	85.89	7.82	0.94	0.13	96.46	4.69	4.50
LIME+SHAP	162	5.51	86.03	7.47	0.94	0.10	92.91	12.54	8.50
LIME	112	5.05	64.79	6.05	0.87	0.13	85.90	10.90	5.38

Table A21 Summary of medians for fusion methods across all metrics.

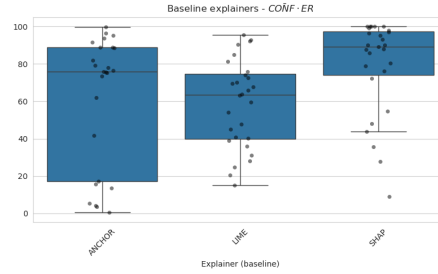
Method	N	\bar{M}	$C\bar{O}N\bar{F} \cdot ER$	$C\bar{O}N\bar{F} \cdot C\bar{O}V \cdot ER$	$C\bar{O}N\bar{F}$	$C\bar{O}V$	ER	$F(\bar{n})$	$Med(F(\bar{n}))$
Lasso global	137	6.53	22.05	7.58	0.66	0.33	46.90	0.80	0.00
Weighted	137	6.15	82.19	11.33	0.90	0.15	93.83	22.74	13.00
Best	57	5.55	96.86	10.00	0.97	0.10	100.00	28.42	26.00
Lasso	137	5.28	91.05	9.35	0.94	0.12	100.00	6.69	6.00
Baseline	80	4.73	76.33	8.94	0.86	0.14	93.75	22.54	20.50
Intersection	57	3.92	51.32	6.29	0.81	0.13	70.00	5.76	1.25
Union	57	1.67	94.49	5.27	0.94	0.06	100.00	42.61	42.00

A.2 Additional Figures

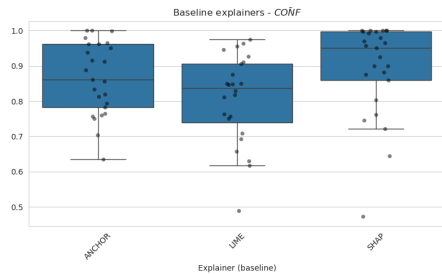
A.2.1 Plots for Baseline (single) Explainers



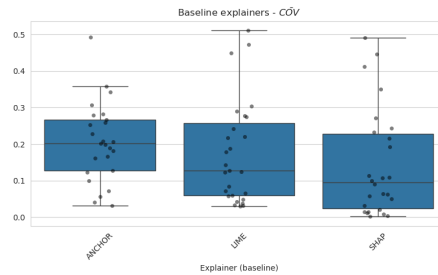
(a) \bar{M} (Objective function)



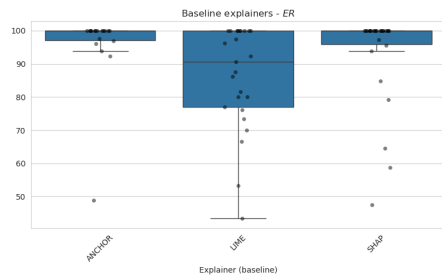
(b) $\overline{\text{CONF}} \cdot ER$ (Avg. Conf.*Expl. R.)



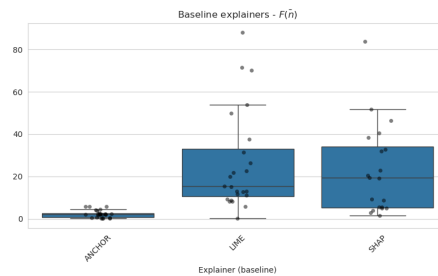
(c) $\overline{\text{CONF}}$ (Average Confidence)



(d) $\overline{\text{COV}}$ (Average Coverage)



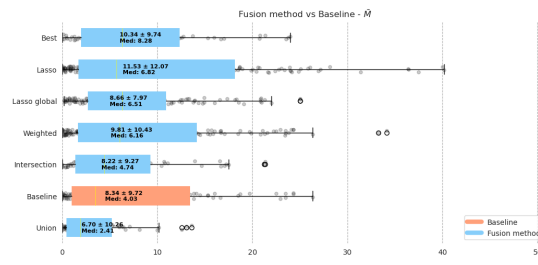
(e) ER (Explained Ratio)



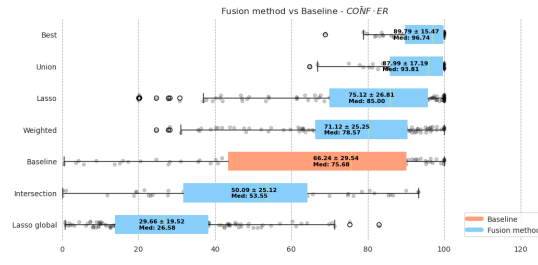
(f) $\overline{F(n)}$ (Average Feature Count)

Fig. A1 Performance comparison of baseline (single) explainers across key metrics. The metrics displayed are: \bar{M} (Objective function), $\overline{\text{CONF}} \cdot ER$ (Average Confidence * Explained Ratio), $\overline{\text{CONF}}$ (Average Confidence), $\overline{\text{COV}}$ (Average Coverage), ER (Explained Ratio), and $\overline{F(n)}$ (Average Feature Count). Each plot visualizes the metric distribution for Anchor, LIME, and SHAP under the baseline condition.

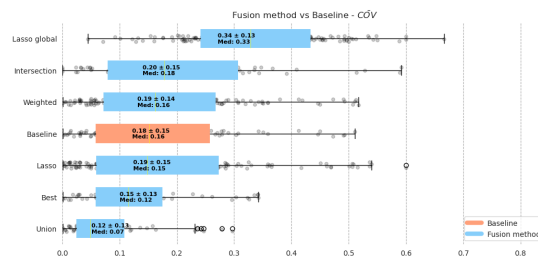
A.2.2 Comparison of Baselines and Fusion Explainers



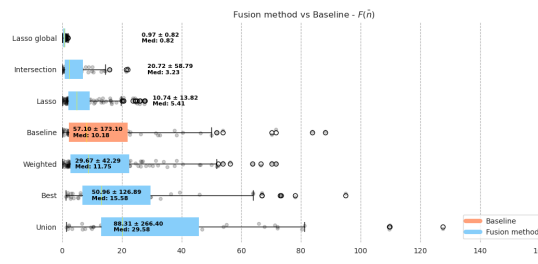
(a) Objective function performance (\bar{M}).



(b) Combined metric $\overline{CONF} \cdot ER$ (Confidence \cdot Explained Ratio).



(c) Metric \overline{COV} (Coverage).



(d) Average feature count ($\bar{F}(n)$).

Fig. A2 Single-explainer baselines (orange) vs fusion methods (blue). Boxplots are annotated with mean, standard deviation, and median. Circles denote outliers.

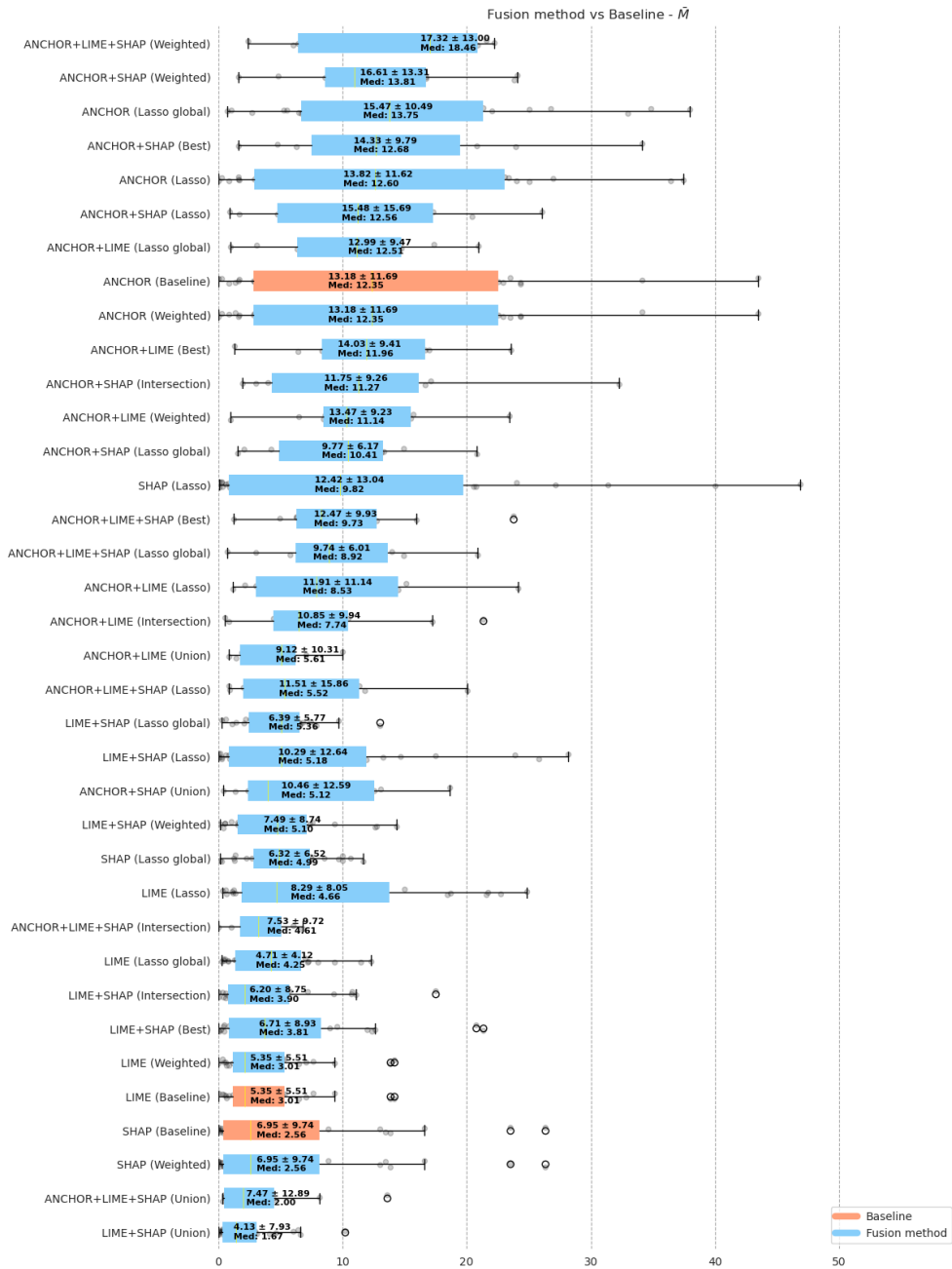


Fig. A3 Objective function performance (\bar{M}): Comparison of single-explainer baselines (orange) and fusion methods (blue). Circles denote outliers.

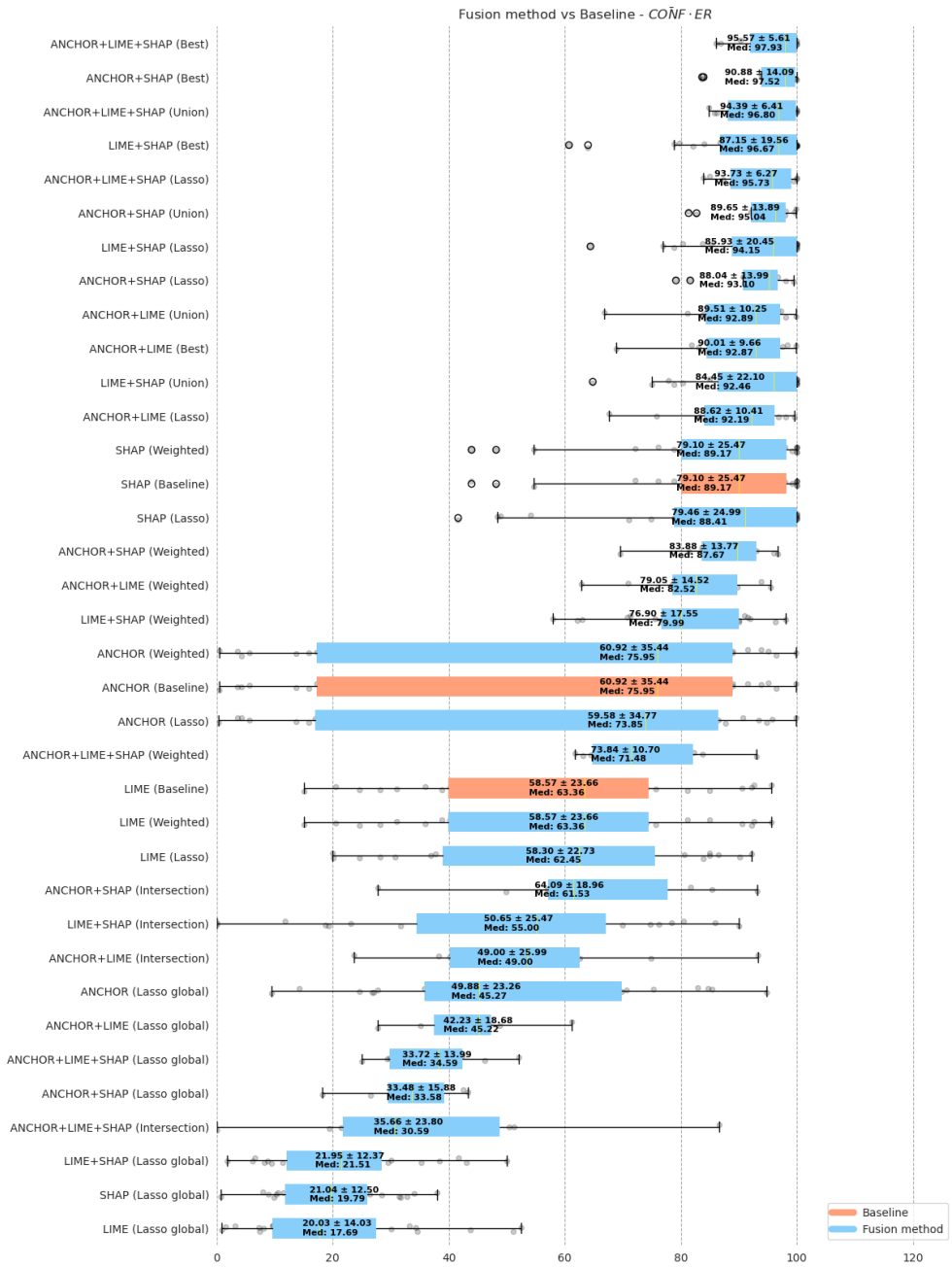


Fig. A4 Combined metric $\overline{CONF} \cdot ER$ (Confidence · Explained Ratio): Comparison of single-explainer baselines (orange) and fusion methods (blue). Circles denote outliers.

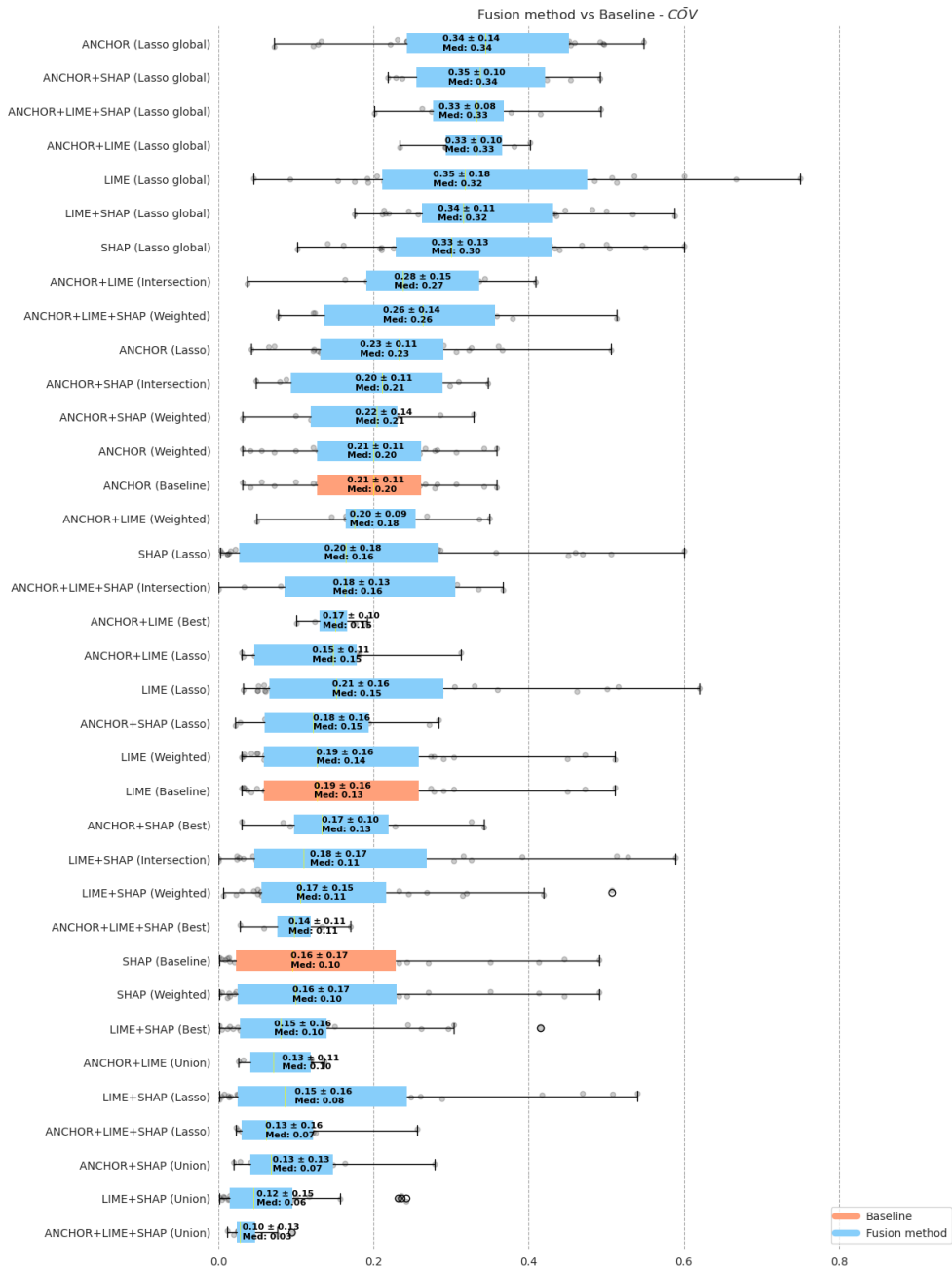
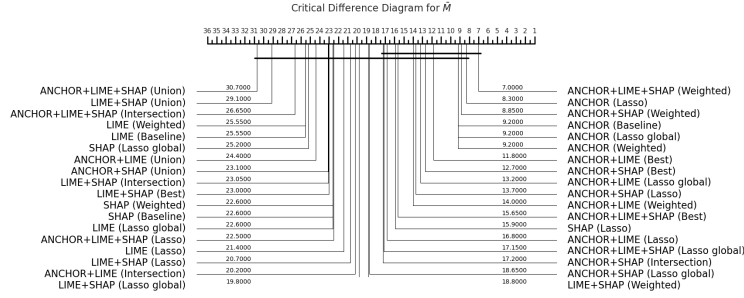


Fig. A5 Metric \overline{COV} (Coverage): Comparison of coverage metrics for single-explainer baselines (orange) and fusion methods (blue). Circles denote outliers.

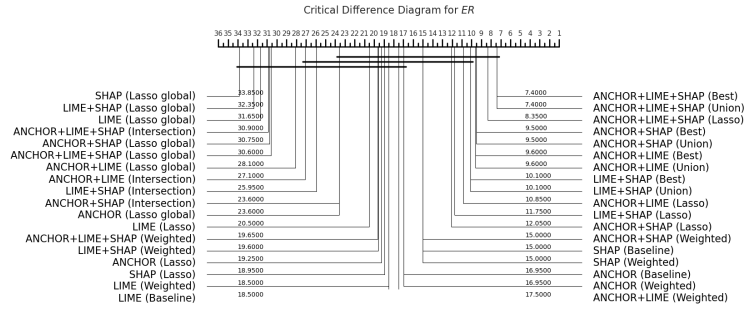


Fig. A6 Average feature count ($F(\bar{n})$): Distribution of feature counts used by single-explainer baselines (orange) and fusion methods (blue). Circles denote outliers.

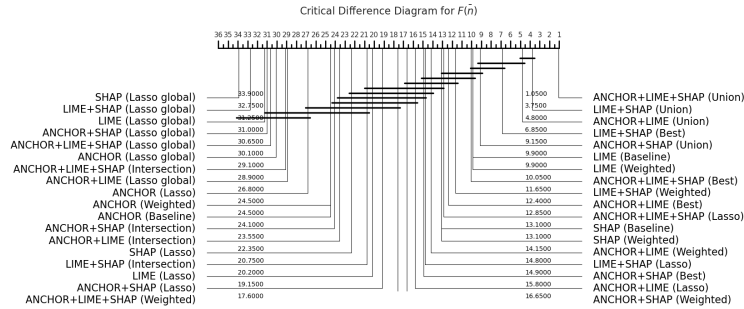
A.2.3 Additional Critical Difference Diagrams



(a) Critical Difference Diagram for \bar{M} (Final Metric).



(b) Critical Difference Diagram for ER (Explained Ratio).



(c) Critical Difference Diagram for $F(\bar{n})$ (Average Feature Count).

Fig. A7 Critical Difference Diagrams for different fusion methods and baselines across metrics. Subfigure (a) shows \bar{M} (Final Metric), (b) illustrates ER (Explained Ratio), and (c) presents $F(\bar{n})$ (Average Feature Count).

A.3 How to read the rules.

Each panel shows the *raw* time series. Red highlights mark time points that satisfy a rule. Dashed vertical lines indicate the start and end of an interval $[\tau_1, \tau_2]$.

For univariate data, a rule is a finite conjunction of point-wise constraints on selected indices t_{j_k} , each constraining the raw value to a half-open interval: $x_{t_{j_k}} \in (\ell_k, u_k]$. For multivariate data, we indicate the feature/channel by a superscript: $x_{t_{j_k}}^{(c_{j_k})} \in (\ell_k, u_k]$. Intervals are obtained by our numeric-to-rules procedure (see Section 3.3).

$$R_i : \begin{cases} x_{t_{j_1}} \in (\ell_1, u_1] \\ x_{t_{j_2}} \in (\ell_2, u_2] \\ \vdots \\ x_{t_{j_m}} \in (\ell_m, u_m] \end{cases} \Rightarrow \begin{cases} \hat{y} = \alpha, \\ \text{CONF}(R_i) = \gamma, \\ \text{COV}(R_i) = \kappa. \end{cases}$$

We report *confidence* (precision) and *coverage* for each rule. Rules are *human-readable proxies of model behaviour*: they show *where* and *what* the classifier relied on, but they are not causal claims. Prototypes and class averages, when shown, give shape context. The figures are *actionable*: a practitioner can verify the inequality on the highlighted segment or inspect the waveform there.

A.4 Dataset-level exemplar visualisations

A.4.1 Dataset-level exemplar visualisations for *ECG200*

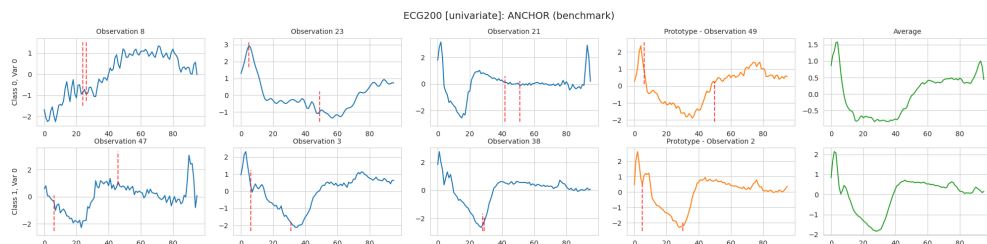
Visualizations intuitively link numeric feature attribution explanations to *TS* structure, aiding interpretability. Our framework transforms numeric explanations into rules consisting of features and intervals of their applicability, which can be visualized on *TS plots* and aid revealing patterns and decision-making.

Figure A8 shows *LIME* and *SHAP* explanations converted into rule-based intervals for *ECG200* dataset (*univariate*, two classes), as well as *Anchor* (native rule-based). Each subplot consists of five plots per row, where each row represents visualizations for one class. The next row contains the second class. The first three columns display green-plotted instances that are maximally diverse, while the fourth column represents the most average, prototypical observation (orange-plotted). The last (green) column shows the class average. Red vertical lines mark feature intervals where time points satisfy rules. *LIME* targets mainly the initial waveform sections, whereas *SHAP* highlights central intervals. *Anchor+LIME+SHAP Lasso fusion* merges both methods, improving coverage and confidence ratio. This slightly increases the median feature count from 4 to 5. Notably, *Observation2* in *Class1*, under-unexplained by *LIME*, is covered by *fusion*. Despite added complexity, *fusion* remains computationally efficient for *TS*.

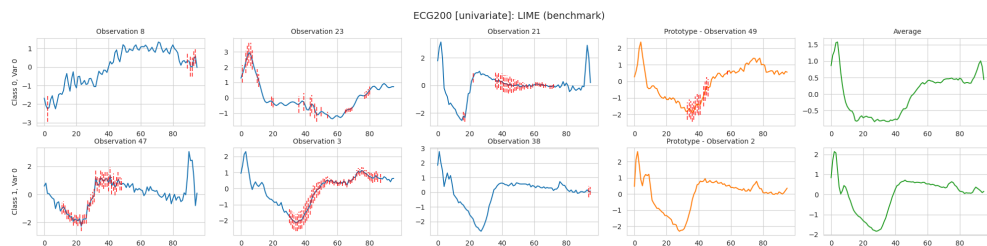
A.4.2 Dataset-level exemplar visualisations for *Plane*

The *Plane* dataset (*univariate*, 6 classes) highlights differences in rule intervals from *Anchor*, *SHAP*, *LIME*, and their *fusion* (Figures A9-A12, Appendix). *Anchor* uses fewer variables, but its red-marked *intervals are often too wide*. This reduces informativeness, as broad intervals fail to capture nuances of *TS* shape. *SHAP* and *LIME* use more variables, while their interval method (Section 3.3) generates *narrower ranges* via multidimensional perturbations. Narrower intervals may improve interpretability

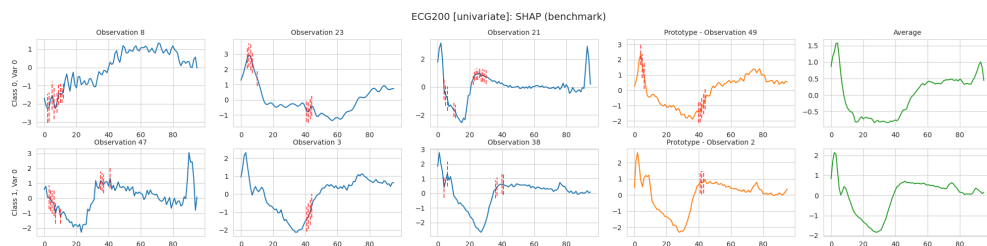
by focusing attention on specific waveform segments. However, overly narrow intervals risk overfitting. Our fusion step trades off precision, coverage, and simplicity to mitigate this. *Fusing Anchor*, *SHAP*, and *LIME* with *"best" method* matches *SHAP*'s baseline performance with significantly fewer variables.



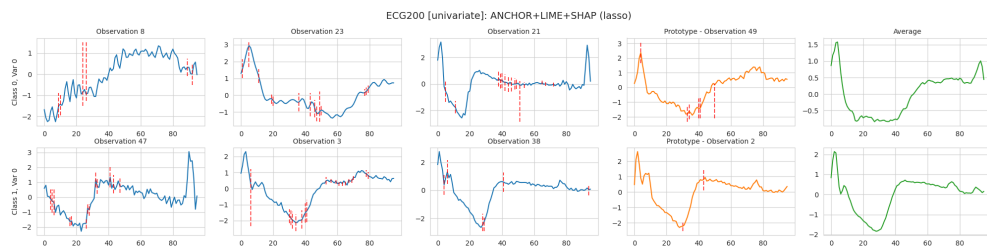
(a) ECG200 with Anchor (baseline)



(b) ECG200 with LIME (baseline)



(c) ECG200 with SHAP (baseline)



(d) ECG200 with Anchor+LIME+SHAP (Lasso fusion)

Fig. A8 Visual explanations for univariate ECG200 data (two classes).

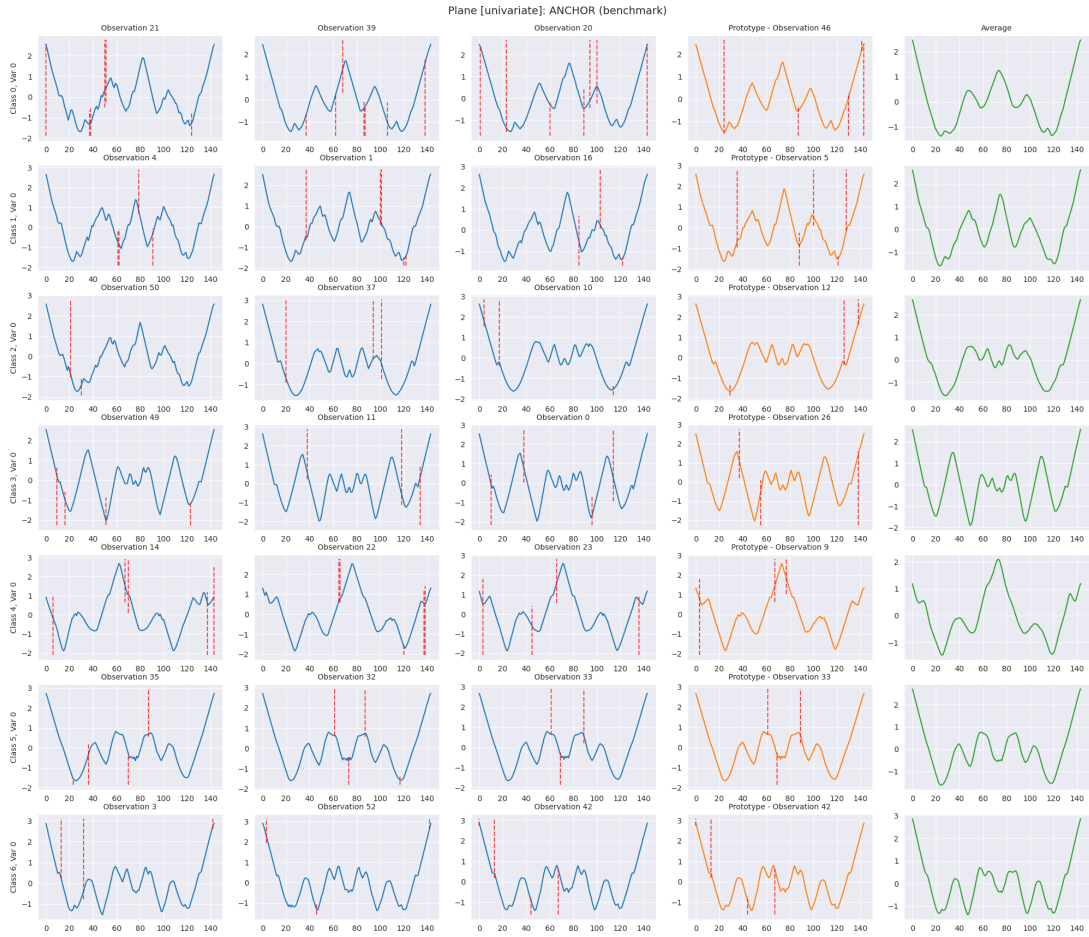


Fig. A9 Plane dataset with Anchor (baseline).

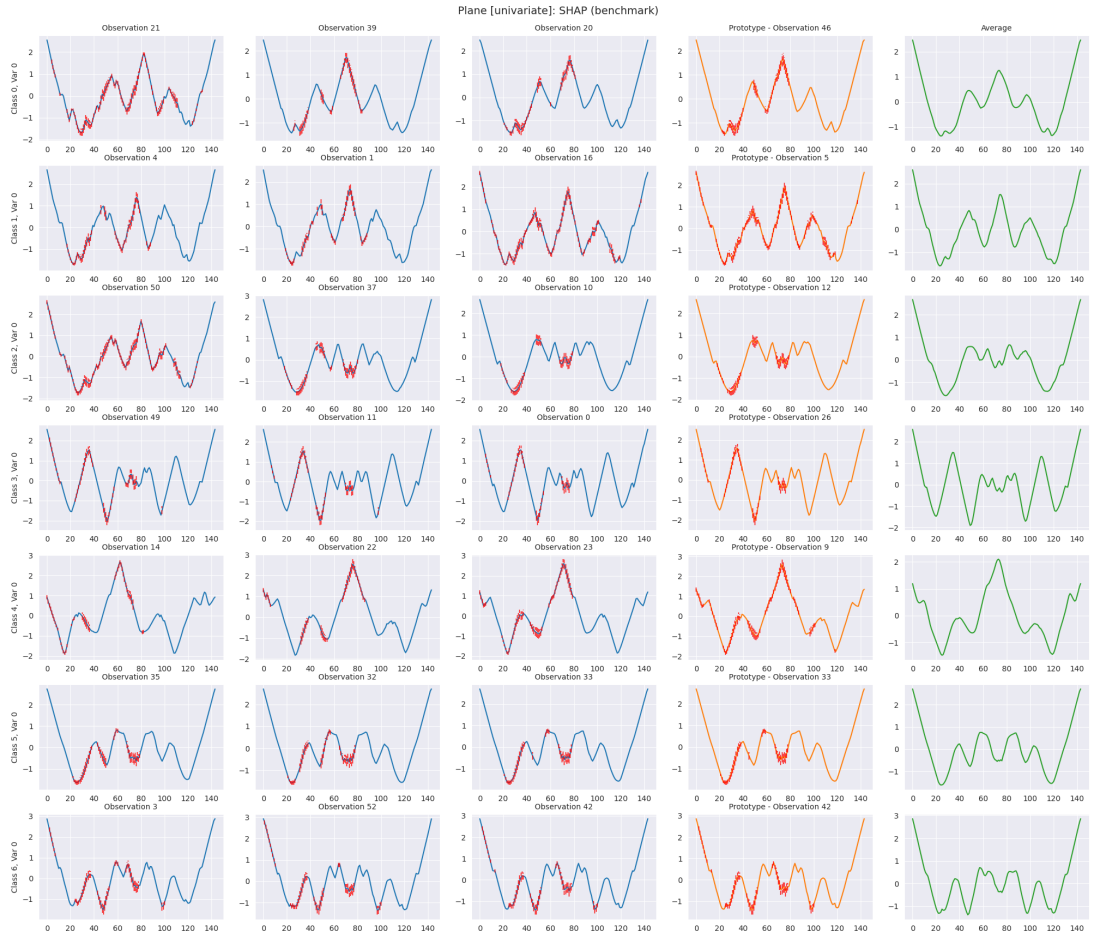


Fig. A10 Plane dataset with SHAP (baseline).

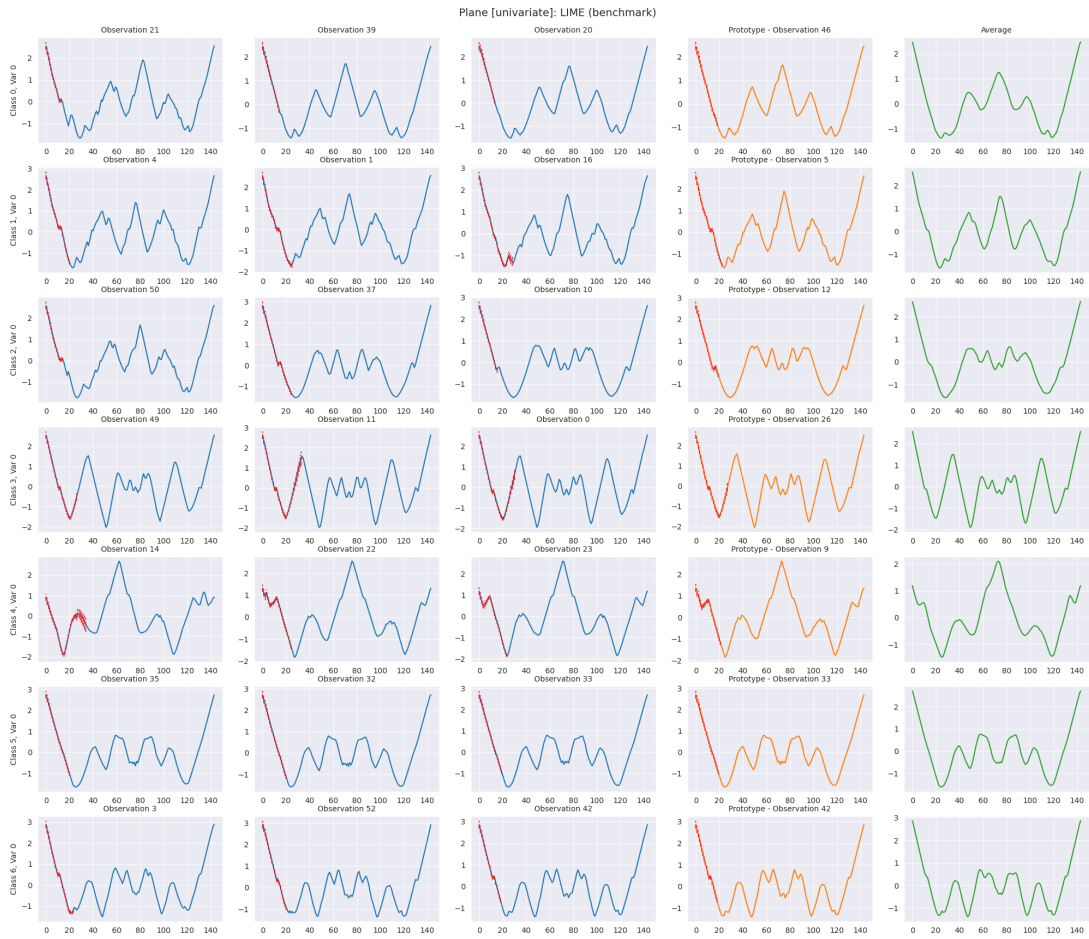


Fig. A11 Plane dataset with LIME (baseline).

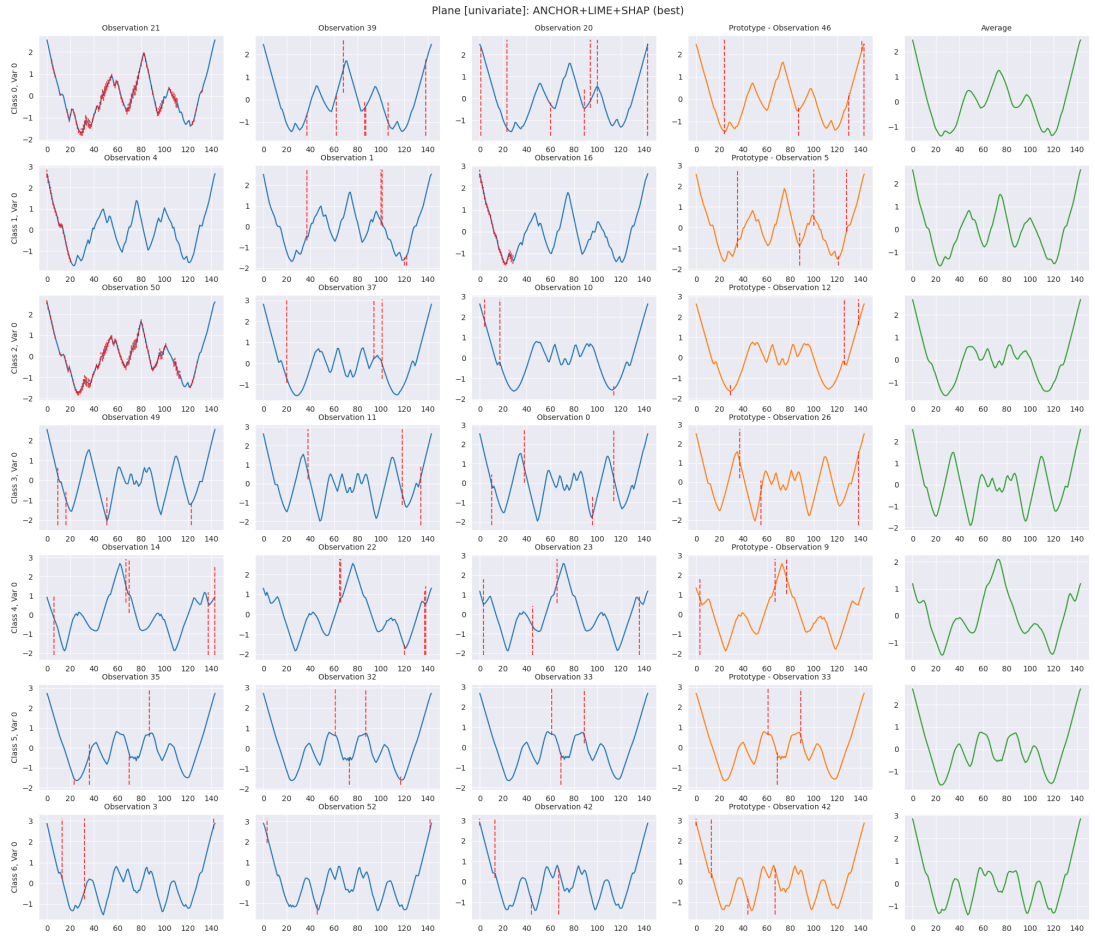


Fig. A12 Plane dataset with Anchor+LIME+SHAP (Best Combination).

B Supplementary Materials

Friedman and Nemenyi: To compare multiple methods statistically, we applied the Friedman test, followed by post-hoc Nemenyi comparisons. The Friedman test results provide insights into the statistical significance of differences across methods. Table B22 reports results at the method level, considering different fusion strategies (e.g., **Baseline**, **Best**, **Intersection**, **Weighted**). Table B23 presents results for all rule sets, accounting for the combinations of explainers they comprise, both single and compound. For pairwise comparisons, we employed the Nemenyi test. The first set of tables, from Table B24 to Table B31, evaluates fusion combinations in terms of explainer types. The second set, from Table B32 to Table B39, focuses on comparisons across fusion methods.

B.1 Friedman Tests

Table B22 Friedman test results for all fusion methods (e.g. **Baseline**, **Best**, **Intersection**, ... , **Weighted**) across metrics.

Metric	χ^2	p
\bar{M}	41.46	< 0.001***
$\overline{CONF} \cdot ER$	130.10	< 0.001***
$\overline{CONF} \cdot \overline{COV} \cdot ER$	29.49	< 0.001***
\overline{CONF}	95.69	< 0.001***
\overline{COV}	110.02	< 0.001***
ER	126.00	< 0.001***
$F(\bar{n})$	136.22	< 0.001***
$Med(F(n))$	128.66	< 0.001***

*p(<0.05), **p(<0.01), ***p(<0.001)

Table B23 Friedman test results for all fused rule sets (taking into account explainers combinations they are composed of, e.g. *Anchor*, *Anchor+LIME*, *Anchor+LIME+SHAP*, etc.) across metrics.

Metric	χ^2	p
\bar{M}	36.09	< 0.001***
$\bar{CONF} \cdot ER$	17.31	0.008**
$\bar{CONF} \cdot \bar{COV} \cdot ER$	30.64	< 0.001***
\bar{CONF}	19.16	0.004**
\bar{COV}	13.50	0.036*
ER	13.41	0.037*
$F(\bar{n})$	27.26	< 0.001***
$Med(F(\bar{n}))$	28.03	< 0.001***
*p(<0.05), **p(<0.01), ***p(<0.001)		

B.2 Nemenyi Tests

Table B24 Nemenyi test results for fusion combinations for \bar{M} . P-values for pairwise comparisons.

Rules Combination	Anchor	Anchor+LIME	Anchor+LIME+SHAP	Anchor+SHAP	LIME	LIME+SHAP	SHAP
Anchor	1.00	0.25	0.023*	0.69	0.001**	0.001**	0.002**
Anchor+LIME	0.25	1.00	0.90	0.90	0.13	0.31	0.63
Anchor+LIME+SHAP	0.023*	0.90	1.00	0.63	0.63	0.87	0.90
Anchor+SHAP	0.69	0.90	0.63	1.00	0.016*	0.06	0.21
LIME	0.001**	0.13	0.63	0.016*	1.00	0.90	0.90
LIME+SHAP	0.001**	0.31	0.87	0.06	0.90	1.00	0.90
SHAP	0.002**	0.63	0.90	0.21	0.90	0.90	1.00

*p(<0.05), **p(<0.01), ***p(<0.001)

Table B25 Nemenyi test results for fusion combinations for $C\bar{O}NF \cdot ER$. P-values for pairwise comparisons.

Rules Combination	Anchor	Anchor+LIME	Anchor+LIME+SHAP	Anchor+SHAP	LIME	LIME+SHAP	SHAP
Anchor	1.00	0.90	0.90	0.69	0.37	0.90	0.90
Anchor+LIME	0.90	1.00	0.56	0.90	0.043*	0.90	0.69
Anchor+LIME+SHAP	0.90	0.56	1.00	0.21	0.87	0.90	0.90
Anchor+SHAP	0.69	0.90	0.21	1.00	0.005**	0.87	0.31
LIME	0.37	0.043*	0.87	0.005**	1.00	0.21	0.75
LIME+SHAP	0.90	0.90	0.90	0.87	0.21	1.00	0.90
SHAP	0.90	0.69	0.90	0.31	0.75	0.90	1.00

*p(<0.05), **p(<0.01), ***p(<0.001)

Table B26 Nemenyi test results for fusion combinations for $C\bar{O}NF \cdot C\bar{O}V \cdot ER$. P-values for pairwise comparisons.

Rules Combination	Anchor	Anchor+LIME	Anchor+LIME+SHAP	Anchor+SHAP	LIME	LIME+SHAP	SHAP
Anchor	1.00	0.87	0.06	0.75	0.004**	0.001**	0.001**
Anchor+LIME	0.87	1.00	0.63	0.90	0.17	0.08	0.08
Anchor+LIME+SHAP	0.06	0.63	1.00	0.75	0.90	0.90	0.90
Anchor+SHAP	0.75	0.90	0.75	1.00	0.25	0.13	0.13
LIME	0.004**	0.17	0.90	0.25	1.00	0.90	0.90
LIME+SHAP	0.001**	0.08	0.90	0.13	0.90	1.00	0.90
SHAP	0.001**	0.08	0.90	0.13	0.90	0.90	1.00

*p(<0.05), **p(<0.01), ***p(<0.001)

Table B27 Nemenyi test results for fusion combinations for \overline{CONF} . P-values for pairwise comparisons.

Rules Combination	Anchor	Anchor+LIME	Anchor+LIME+SHAP	Anchor+SHAP	LIME	LIME+SHAP	SHAP
Anchor	1.00	0.90	0.90	0.50	0.31	0.90	0.90
Anchor+LIME	0.90	1.00	0.90	0.90	0.043*	0.90	0.90
Anchor+LIME+SHAP	0.90	0.90	1.00	0.90	0.043*	0.90	0.90
Anchor+SHAP	0.50	0.90	0.90	1.00	0.001**	0.90	0.50
LIME	0.31	0.043*	0.043*	0.001**	1.00	0.043*	0.31
LIME+SHAP	0.90	0.90	0.90	0.90	0.043*	1.00	0.90
SHAP	0.90	0.90	0.90	0.50	0.31	0.90	1.00

*p(<0.05), **p(<0.01), ***p(<0.001)

Table B28 Nemenyi test results for fusion combinations for \overline{COV} . P-values for pairwise comparisons.

Rules Combination	Anchor	Anchor+LIME	Anchor+LIME+SHAP	Anchor+SHAP	LIME	LIME+SHAP	SHAP
Anchor	1.00	0.44	0.13	0.31	0.17	0.011*	0.13
Anchor+LIME	0.44	1.00	0.90	0.90	0.90	0.75	0.90
Anchor+LIME+SHAP	0.13	0.90	1.00	0.90	0.90	0.90	0.90
Anchor+SHAP	0.31	0.90	0.90	1.00	0.90	0.87	0.90
LIME	0.17	0.90	0.90	0.90	1.00	0.90	0.90
LIME+SHAP	0.011*	0.75	0.90	0.87	0.90	1.00	0.90
SHAP	0.13	0.90	0.90	0.90	0.90	0.90	1.00

*p(<0.05), **p(<0.01), ***p(<0.001)

Table B29 Nemenyi test results for fusion combinations for \overline{ER} . P-values for pairwise comparisons.

Rules Combination	Anchor	Anchor+LIME	Anchor+LIME+SHAP	Anchor+SHAP	LIME	LIME+SHAP	SHAP
Anchor	1.00	0.90	0.50	0.90	0.31	0.90	0.63
Anchor+LIME	0.90	1.00	0.44	0.90	0.25	0.90	0.56
Anchor+LIME+SHAP	0.50	0.44	1.00	0.25	0.90	0.87	0.90
Anchor+SHAP	0.90	0.90	0.25	1.00	0.13	0.90	0.37
LIME	0.31	0.25	0.90	0.13	1.00	0.69	0.90
LIME+SHAP	0.90	0.90	0.87	0.90	0.69	1.00	0.90
SHAP	0.63	0.56	0.90	0.37	0.90	0.90	1.00

*p(<0.05), **p(<0.01), ***p(<0.001)

Table B30 Nemenyi test results for fusion combinations for $\overline{F(n)}$. P-values for pairwise comparisons.

Rules Combination	Anchor	Anchor+LIME	Anchor+LIME+SHAP	Anchor+SHAP	LIME	LIME+SHAP	SHAP
Anchor	1.00	0.023*	0.016*	0.56	0.016*	0.001**	0.50
Anchor+LIME	0.023*	1.00	0.90	0.75	0.90	0.75	0.81
Anchor+LIME+SHAP	0.016*	0.90	1.00	0.69	0.90	0.81	0.75
Anchor+SHAP	0.56	0.75	0.69	1.00	0.69	0.06	0.90
LIME	0.016*	0.90	0.90	0.69	1.00	0.81	0.75
LIME+SHAP	0.001**	0.75	0.81	0.06	0.81	1.00	0.08
SHAP	0.50	0.81	0.75	0.90	0.75	0.08	1.00

*p(<0.05), **p(<0.01), ***p(<0.001)

Table B31 Nemenyi test results for fusion combinations for $Med(F(n))$. P-values for pairwise comparisons.

Rules Combination	Anchor	Anchor+LIME	Anchor+LIME+SHAP	Anchor+SHAP	LIME	LIME+SHAP	SHAP
Anchor	1.00	0.31		0.011*	0.78	0.050*	0.001**
Anchor+LIME	0.31	1.00		0.87	0.90	0.90	0.13
Anchor+LIME+SHAP	0.011*	0.87		1.00	0.40	0.90	0.81
Anchor+SHAP	0.78	0.90		1.00	0.69	0.014*	0.90
LIME	0.050*	0.90		0.90	1.00	0.53	0.90
LIME+SHAP	0.001**	0.13		0.81	0.014*	1.00	0.08
SHAP	0.44	0.90		0.75	0.90	0.90	1.00

*p(<0.05), **p(<0.01), ***p(<0.001)

Table B32 Nemenyi test results for fusion methods for \bar{M} . P-values for pairwise comparisons.

Method	Baseline	Best	Intersection	Lasso	Lasso global	Union	Weighted
Baseline	1.00	0.015*	0.56	0.49	0.56	0.90	0.90
Best	0.015*	1.00	0.001**	0.001**	0.001**	0.001**	0.018*
Intersection	0.56	0.001**	1.00	0.90	0.90	0.90	0.53
Lasso	0.49	0.001**	0.90	1.00	0.90	0.90	0.45
Lasso global	0.56	0.001**	0.90	0.90	1.00	0.90	0.53
Union	0.90	0.001**	0.90	0.90	0.90	1.00	0.90
Weighted	0.90	0.018*	0.53	0.45	0.53	0.90	1.00

*p(<0.05), **p(<0.01), ***p(<0.001)

Table B33 Nemenyi test results for fusion methods for $C\bar{O}N\bar{F} \cdot ER$. P-values for pairwise comparisons.

Method	Baseline	Best	Intersection	Lasso	Lasso global	Union	Weighted
Baseline	1.00	0.001**	0.21	0.001**	0.47	0.001**	0.80
Best	0.001**	1.00	0.003**	0.33	0.001**	0.90	0.001**
Intersection	0.21	0.003**	1.00	0.64	0.001**	0.001**	0.90
Lasso	0.001**	0.33	0.64	1.00	0.001**	0.020*	0.11
Lasso global	0.47	0.001**	0.001**	0.001**	1.00	0.001**	0.018*
Union	0.001**	0.90	0.001**	0.020*	0.001**	1.00	0.001**
Weighted	0.80	0.001**	0.90	0.11	0.018*	0.001**	1.00

*p(<0.05), **p(<0.01), ***p(<0.001)

Table B34 Nemenyi test results for fusion methods for $C\bar{O}N\bar{F} \cdot C\bar{O}V \cdot ER$. P-values for pairwise comparisons.

Method	Baseline	Best	Intersection	Lasso	Lasso global	Union	Weighted
Baseline	1.00	0.90	0.008**	0.18	0.37	0.10	0.64
Best	0.90	1.00	0.001**	0.013*	0.044*	0.006**	0.14
Intersection	0.008**	0.001**	1.00	0.90	0.75	0.90	0.49
Lasso	0.18	0.013*	0.90	1.00	0.90	0.90	0.90
Lasso global	0.37	0.044*	0.75	0.90	1.00	0.90	0.90
Union	0.10	0.006**	0.90	0.90	0.90	1.00	0.90
Weighted	0.64	0.14	0.49	0.90	0.90	0.90	1.00

*p(<0.05), **p(<0.01), ***p(<0.001)

Table B35 Nemenyi test results for fusion methods for $C\bar{O}N\bar{F}$. P-values for pairwise comparisons.

Method	Baseline	Best	Intersection	Lasso	Lasso global	Union	Weighted
Baseline	1.00	0.001**	0.14	0.016*	0.90	0.001**	0.90
Best	0.001**	1.00	0.14	0.54	0.001**	0.77	0.001**
Intersection	0.14	0.14	1.00	0.90	0.004**	0.001**	0.35
Lasso	0.016*	0.54	0.90	1.00	0.001**	0.022*	0.06
Lasso global	0.90	0.001**	0.004**	0.001**	1.00	0.001**	0.65
Union	0.001**	0.77	0.001**	0.022*	0.001**	1.00	0.001**
Weighted	0.90	0.001**	0.35	0.06	0.65	0.001**	1.00

*p(<0.05), **p(<0.01), ***p(<0.001)

Table B36 Nemenyi test results for fusion methods for $C\bar{O}V$. P-values for pairwise comparisons.

Method	Baseline	Best	Intersection	Lasso	Lasso global	Union	Weighted
Baseline	1.00	0.001**	0.65	0.90	0.001**	0.23	0.90
Best	0.001**	1.00	0.001**	0.001**	0.001**	0.35	0.001**
Intersection	0.65	0.001**	1.00	0.75	0.008**	0.002**	0.90
Lasso	0.90	0.001**	0.75	1.00	0.001**	0.16	0.90
Lasso global	0.001**	0.001**	0.008**	0.001**	1.00	0.001**	0.001**
Union	0.23	0.35	0.002**	0.16	0.001**	1.00	0.016*
Weighted	0.90	0.001**	0.90	0.90	0.001**	0.016*	1.00

*p(<0.05), **p(<0.01), ***p(<0.001)

Table B37 Nemenyi test results for fusion methods for ER . P-values for pairwise comparisons.

Method	Baseline	Best	Intersection	Lasso	Lasso global	Union	Weighted
Baseline	1.00	0.001**	0.49	0.001**	0.69	0.001**	0.39
Best	0.001**	1.00	0.001**	0.13	0.001**	0.90	0.001**
Intersection	0.49	0.001**	1.00	0.29	0.011*	0.001**	0.90
Lasso	0.001**	0.13	0.29	1.00	0.001**	0.13	0.39
Lasso global	0.69	0.001**	0.011*	0.001**	1.00	0.001**	0.006**
Union	0.001**	0.90	0.001**	0.13	0.001**	1.00	0.001**
Weighted	0.39	0.001**	0.90	0.39	0.006**	0.001**	1.00

*p(<0.05), **p(<0.01), ***p(<0.001)

Table B38 Nemenyi test results for fusion methods for $F(\bar{n})$. P-values for pairwise comparisons.

Method	Baseline	Best	Intersection	Lasso	Lasso global	Union	Weighted
Baseline	1.00	0.001**	0.10	0.90	0.10	0.001**	0.027*
Best	0.001**	1.00	0.001**	0.001**	0.001**	0.20	0.001**
Intersection	0.10	0.001**	1.00	0.11	0.001**	0.29	0.90
Lasso	0.90	0.001**	0.11	1.00	0.08	0.001**	0.033*
Lasso global	0.10	0.001**	0.001**	0.08	1.00	0.001**	0.001**
Union	0.001**	0.20	0.29	0.001**	0.001**	1.00	0.56
Weighted	0.027*	0.001**	0.90	0.033*	0.001**	0.56	1.00

*p(<0.05), **p(<0.01), ***p(<0.001)

Table B39 Nemenyi test results for fusion methods for $Med(F(n))$. P-values for pairwise comparisons.

Method	Baseline	Best	Intersection	Lasso	Lasso global	Union	Weighted
Baseline	1.00	0.001**	0.05	0.49	0.43	0.001**	0.005**
Best	0.001**	1.00	0.001**	0.001**	0.001**	0.20	0.001**
Intersection	0.05	0.001**	1.00	0.90	0.001**	0.18	0.90
Lasso	0.49	0.001**	0.90	1.00	0.002**	0.009**	0.58
Lasso global	0.43	0.001**	0.001**	0.002**	1.00	0.001**	0.001**
Union	0.001**	0.20	0.18	0.009**	0.001**	1.00	0.56
Weighted	0.005**	0.001**	0.90	0.58	0.001**	0.56	1.00

*p(<0.05), **p(<0.01), ***p(<0.001)